The influence of observed cirrus microphysical properties on shortwave radiation: A case study over Oklahoma

Päivi Mauno,[1] Greg M. McFarquhar,[2] Petri Räisänen,[3] Michael Kahnert,[4] Michael S. Timlin,[5] and Timo Nousiainen[1]

Received 1 April 2011; revised 8 September 2011; accepted 7 October 2011; published 22 November 2011.

[1] The shortwave radiative effect of an ice cloud observed over the Atmospheric Radiation Measurement program's Southern Great Plains site in Oklahoma is investigated. Airborne microphysical data from a cloud particle imager, optical array probes, and forward scattering probes are used to construct vertical profiles of the size and shape distributions of ice crystals. Due to uncertainties associated with measuring the sizes and shapes of small ice crystals with maximum dimensions less than 120 μm, five alternate size-shape distributions are derived and combined with existing databases of wavelength-dependent single-scattering properties of idealized ice crystals to obtain vertical profiles of optical properties. The dependence of the surface and the top-of-the-atmosphere fluxes on these uncertainties is simulated with a radiative transfer model. In addition, surface fluxes are compared against measurements at the surface. It is found that the differences between the modeled and measured fluxes are too large to be explained by uncertainties in the shape and concentrations of small ice crystals. Sensitivity tests suggest that the discrepancies occur because the real optical thickness is larger than that derived from the aircraft profiles most of the time. When the optical thickness was derived based on modeled and measured direct fluxes, the modeled total downward flux agreed well with the measurements. Slightly (less than 10%) reducing the asymmetry parameter, which is possibly associated with the presence of surface roughness, air bubble inclusions or other nonidealities in ice crystals, may further improve the agreement with observations.

Citation: Mauno, P., G. M. McFarquhar, P. Räisänen, M. Kahnert, M. S. Timlin, and T. Nousiainen (2011), The influence of observed cirrus microphysical properties on shortwave radiation: A case study over Oklahoma, *J. Geophys. Res.*, *116*, D22208, doi:10.1029/2011JD016058.

1. Introduction

[2] Tropospheric ice clouds, such as cirrus clouds, are globally distributed and cover about 30 percent of the globe at any given time [*Wylie and Menzel*, 1999; *Stubenrauch et al.*, 2006]. These clouds are an important component in the Earth-atmosphere system through their impact on the top-of-the-atmosphere (TOA) and surface radiation budgets as well as through their contributions to diabatic heating in the upper troposphere [*Ramaswamy and Ramanathan*, 1989]. To accurately quantify the radiative effect of ice clouds, the size and shape distributions as well as the possible internal structure of the constituent ice particles, and the horizontal extent and vertical structure of the cloud, must be known. Such a complete characterization of ice clouds is not currently available for climate models. For this reason, bulk parameters describing the size and shape distributions, such as an effective radius of ice crystals [e.g., *McFarquhar et al.*, 2003] must either be prescribed or parameterized. It is difficult to account for the effect of ice particle shape and composition in parameterizations of single-scattering properties for climate models owing to the large number of different ice particle morphologies [*McFarquhar et al.*, 2002]. However, it is known that morphology can significantly affect the radiative impact of cirrus clouds [e.g., *Kahnert et al.*, 2008]. Several studies have developed alternate parameterizations of ice clouds that can be employed in climate models that have used hexagonal shapes to represent the ice crystals [*Ebert and Curry*, 1992; *Fu*, 1996; *Fu et al.*, 1998], or different parameterizations to represent different shapes of ice crystals [*Wyser and Yang*, 1998; *Kristjánsson et al.*, 1999] or parameterizations with the single-scattering properties weighted according to the frequency of occurrence of different sizes and shapes of ice crystals [*McFarquhar et al.*, 2002; *Hong et al.*, 2009].

[1]Department of Physics, University of Helsinki, Helsinki, Finland.
[2]Department of Atmospheric Sciences, University of Illinois at Urbana-Champaign, Urbana, Illinois, USA.
[3]Climate Change Research, Finnish Meteorological Institute, Helsinki, Finland.
[4]Swedish Meteorological and Hydrological Institute, Norrköping, Sweden.
[5]Midwestern Regional Climate Center, CAS/ISWS/INRS, University of Illinois at Urbana-Champaign, Champaign, Illinois, USA.

Copyright 2011 by the American Geophysical Union.
0148-0227/11/2011JD016058

Table 1. The Time and Altitude Ranges of the Two Flight Profiles

Profile	GMT	Minimum Altitude (km)	Maximum Altitude (km)
A	18:42–18:55	6.8	8.8
B	21:50–22:15:40	4.7	7.9

[3] Another uncertainty in the development of these parameterizations is the contributions that small ice crystals, hereafter those with maximum dimensions D less than 120 μm, make to the mass and optical properties of cirrus. Studies using forward scattering spectrometer probes (FSSPs) suggest that small ice crystals make substantial contributions to the mass and optical properties [e.g., *Knollenberg et al.*, 1993; *Ivanova et al.*, 2001; *Garrett et al.*, 2003]. However, impactor probes and formvar replicators show small-crystal concentrations much less than those of colocated FSSPs [*Gardiner and Hallett*, 1985; *McFarquhar and Heymsfield*, 1996]. Thus, it has been hypothesized that large ice particles shatter into smaller fragments when they hit the inlets or tips of such probes, artificially inflating the concentrations of small ice crystals [*Gardiner and Hallett*, 1985; *Korolev and Isaac*, 2005; *McFarquhar et al.*, 2007; *Korolev et al.*, 2011; *Lawson*, 2011]. Attempts to characterize the effect of shattering on cloud properties [e.g., *Gayet et al.*, 1996; *Field et al.*, 2003, 2006; *Vidaurre and Hallett*, 2009; *Jensen et al.*, 2009; *Shcherbakov et al.*, 2010] have varied by a wide range, showing that large uncertainties exist in the concentrations of small ice crystals. There are additional uncertainties in the shapes of small ice crystals, as the shapes of these particles cannot be imaged accurately with present imaging probes. Accordingly, different shape models (spheres, Gaussian random spheres, droxtals, Chebyshev particles, and budding bucky balls) have been proposed for these crystals [*McFarquhar et al.*, 2002; *Nousiainen and McFarquhar*, 2004; *Yang et al.*, 2003; *Um and McFarquhar*, 2011].

[4] Shortwave radiances are sensitive to both particle shapes and sizes, but their relative importance appears to depend on the case. For example, using observations from midlatitude and tropical cirrus, *Macke et al.* [1998] and *Schlimme et al.* [2005] showed that the correct particle shape was more important than the correct size distribution from a broadband solar radiative transfer point of view. *McFarquhar et al.* [1999], on the other hand, did not find shape to be significantly more important than size; they also concluded that uncertainties in cloud base and cloud evolution prevented comparisons with multichannel radiometric observations made directly above the in situ cloud observations during the Central Equatorial Pacific Experiment (CEPEX). *Zhang et al.* [1999] also found that modeled radiative fluxes are sensitive to microphysical parameters, with more realistic radiances obtained in experiments where the representation of microphysics is most complete. *Baran and Francis* [2004] noted that simultaneous radiance measurements from both the solar and infrared are important for testing ice scattering models. Clearly, comparisons of observed and simulated radiances using observations from cloud fields are still needed.

[5] In this paper, the shortwave (SW) radiative effect of an ice cloud is modeled using in situ measured size and shape distributions of ice crystals observed during 13 March 2000 in the vicinity of the Atmospheric Radiation Measurement (ARM) program's Southern Great Plains (SGP) site in north central Oklahoma. This work extends previous studies by conducting sensitivity studies that examine the impact of the concentration and morphology of small ice crystals (D < 120 μm) on cloud radiative properties and modeled radiative fluxes, and by directly comparing simulations with measured radiative fluxes at the surface. To describe the shape of ice crystals realistically, 10 different habits are used. Based on the measurements, ice crystals with D > 120 μm are divided into seven habits: column, plate, bullet rosette, budding bullet rosette, spherical, and small and big irregular. The shape of small ice crystals is approximated by using either Gaussian random spheres, droxtals or Chebyshev particles.

[6] In section 2, the observational data are described. In section 3, the in situ data and preexisting databases of ice crystal single-scattering properties are combined to obtain vertical profiles of volume-averaged optical properties, namely the extinction coefficient, the asymmetry parameter, and the single-scattering albedo. The radiative transfer model used is briefly introduced in section 4 and the simulated SW fluxes at the surface and at the top of the atmosphere are presented in section 5. Finally, the conclusions are summarized in section 6.

2. Measurements

[7] In situ cloud measurements were obtained in the vicinity of the United States Department of Energy's Atmospheric Radiation Measurement (DOE ARM) program's Southern Great Plains site in Ponca City, during the March 2000 Cloud Intensive Operational Period (IOP) [*Dong et al.*, 2002; *Heymsfield and Miloshevich*, 2003]. During the IOP, cirrus was sampled by the University of North Dakota (UND) Citation aircraft on five research flights on 4 different days (5 March, 9 March, 12 March, and 13 March). The 13 March flight was selected for further analysis because the ground-based radiation measurements suggested that the cirrus appeared to be the most long-lived and homogeneous among the five different flights. In addition, the pilot notes for this date indicated that the cloud was fairly uniform. During that flight, four vertical profiles were flown by the UND Citation, but only two extended through most of the cloud layer. The measurement times (Greenwich Mean Time, GMT) and corresponding altitude ranges of the profiles used in this study are shown in Table 1.

[8] Data from a vertically pointing millimeter cloud radar (MMCR) operating at a frequency of 35 GHz [*Widener and Johnson*, 2005] at the SGP central facility were used to establish the extent and structure of the cirrus cloud. Figure 1 shows a time-height profile obtained by the MMCR. It can be seen that the cirrus persisted over the radar for more than 6 h. The green (profile A), violet, blue, and black (profile B) lines indicate the altitudes sampled by the UND Citation as a function of time, with the spiral descent flown for profile B covering almost the whole cloud from top to bottom. However, as the UND Citation did not fly directly over the radar, it did not sample exactly the part of the cloud indicated in Figure 1. The location of the radar and the projected flight paths of profiles A and B are illustrated in Figure 2. The distance between the center of spiral B and the radar is about 12 km while for profile A the distance varies from few to

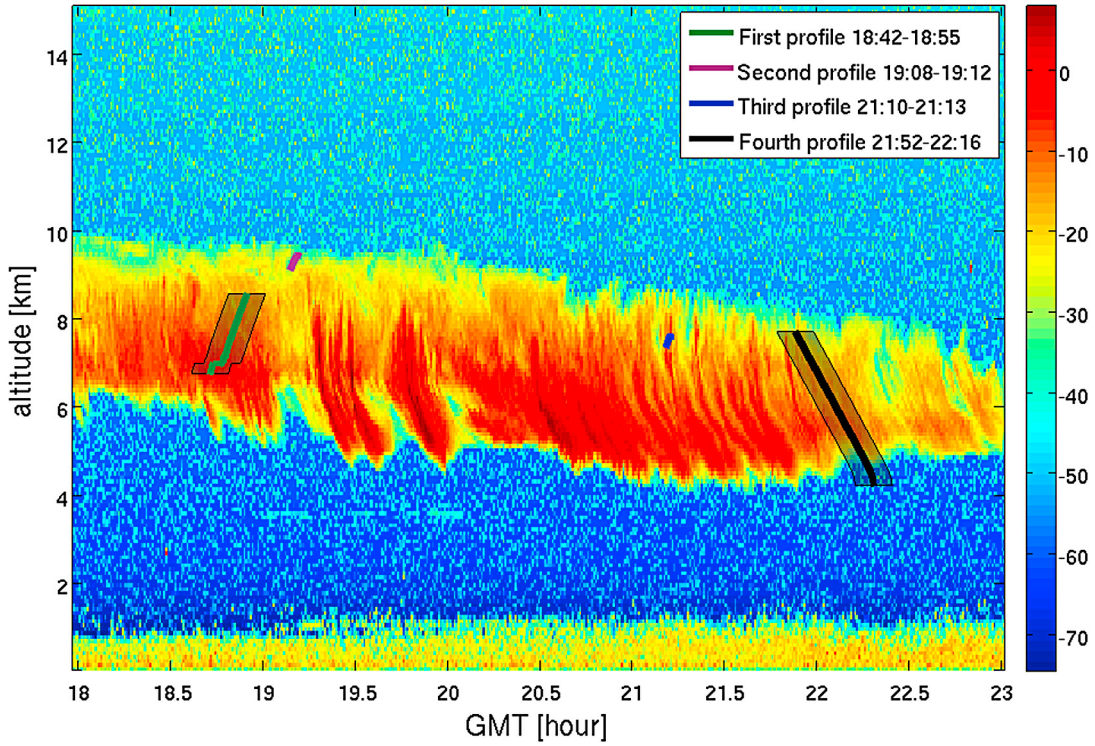

Figure 1. MMCR cloud reflectivity (dBZ) obtained on 13 March 2000 at the SGP central facility at the time of the UND Citation flight. The flight paths of profiles A and B are shown as green and black lines, respectively. The shading around the lines indicates a ±6 min time interval corresponding to that part of the cloud field that might have been sampled by the UND Citation if its distance had been at maximum 10 km to downwind or upwind from the location of the radar. This estimate is based on cloud advection as approximated from radiosonde wind measurements.

over 50 km. To estimate cloud advection, data from two radiosondes released at the central facility on 13 March at 17:29 and 20:30 GMT are used. Given the horizontal extent of the cirrus, it is almost certain that both radiosondes ascended through the cirrus layer, but not at the exact location of the in situ measurements. Based on the radiosondes, the mean wind direction at altitudes between 5 and 10 km was from the northwest and the average wind speed was about 29 ms^{-1}. The mean wind direction and the locations of the radar and the UND during profile B indicate that the exact same part of the cirrus that profile B measured did not advect over the location of the radar. However, part of the cirrus that was measured by UND in the very beginning of the profile A could have passed over the radar a few minutes later. Similarly, the cirrus sampled in the middle of profile A could have been over the radar 10 min earlier. Thus, the gray shading in Figure 1 indicates those portions of the cloud that the UND Citation might have sampled when compensating for advection and assuming the MMCR was directly 10 km down/up of the in situ observations.

[9] In situ vertical profiles of temperature and dew point temperature from the two radiosondes are shown in Figure 3. Inside the cirrus between 5 and 10 km, the temperature in the two soundings differs at most by 1.3 K and the dew point temperature by at most 2.3 K, except for a much larger difference of up to 16 K in dew point temperature between 5 and 5.5 km. Based on the temperature profiles and the MMCR data in Figure 1, this corresponds to the approximate cloud base below which the ice crystals would sublimate.

2.1. Size-Shape Distribution

[10] The UND Citation housed a suite of microphysical probes that measured the size and shape distributions of ice crystals, bulk water contents, and state parameters. In particular, data from a Forward Scattering Spectrometer Probe (FSSP), a one-dimensional cloud probe (1DC), and a two-dimensional cloud probe (2DC) were used in this study to characterize the ice crystals in size ranges of $D < 50$ μm, 50 μm $< D <$ 120 μm, and $D >$ 120 μm, respectively. Although the FSSP is designed for measuring the size distribution of water droplets, it has been used in past studies to determine size distributions of ice crystals [e.g., *Knollenberg et al.*, 1993]. However, as shown by *Jensen et al.* [2009] and *McFarquhar et al.* [2011], remnants of large ice crystals shattering on the shroud, inlet, and tips of this probe can dominate its response so that FSSP concentrations should only be regarded as a large upper bound on small crystal concentrations [e.g., *McFarquhar et al.*, 2003]. The 1DC and 2DC may also suffer from the influence of shattered artifacts [*Korolev et al.*, 2011], especially for particles with $D < 500$ μm, but they are the only probes that measured in this size range ($D > 50$ μm) during the Cloud IOP. The size distributions were computed for a 10 s averaging interval, representing a balance between fine vertical resolution and having enough particles to obtain statistically significant

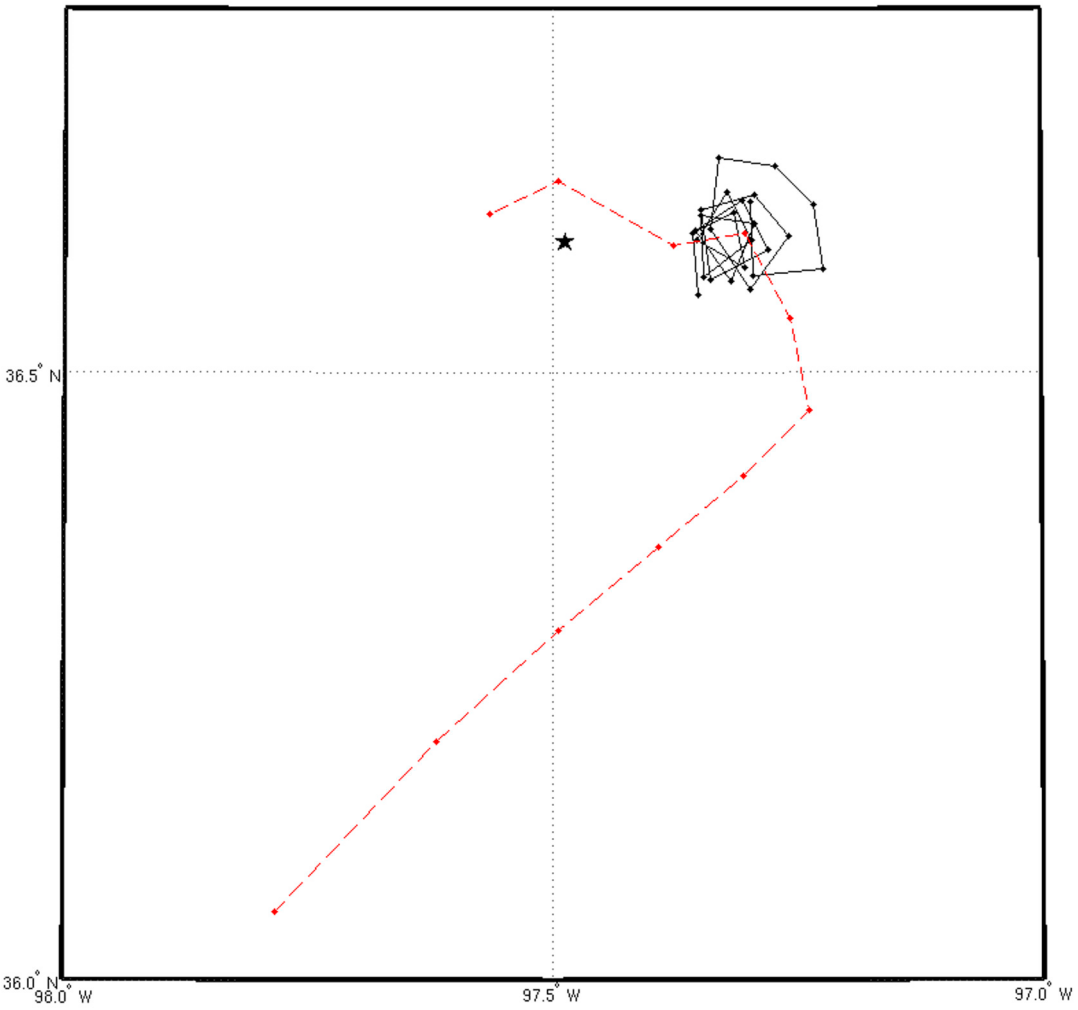

Figure 2. Horizontal flight paths shown for the horizontally ramped ascent (profile A, dashed line) and for the descent spiral (profile B, solid line). The SGP central facility is marked with a star.

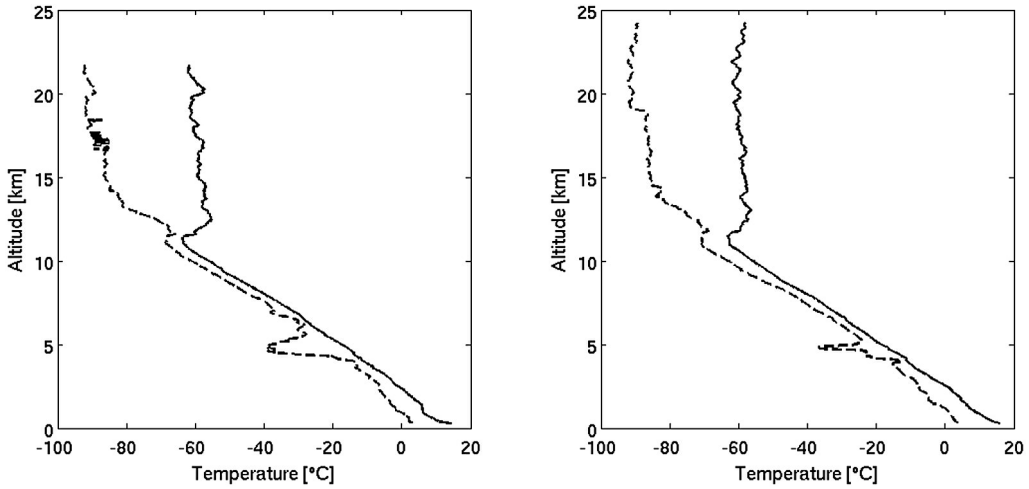

Figure 3. Vertical profiles of temperature (solid line) and dew point temperature (dashed line) obtained from atmospheric soundings released at the SGP central facility on 13 March 2000 at (left) 17:29 and (right) 20:30 GMT.

samples [see *Hallett*, 2003]. A Cloud Particle Imager (CPI) installed on the UND Citation provides high-resolution (2.3 μm) images of ice crystals. Because of its small and as of yet poorly defined sample volume, the CPI was only used to identify the shape of ice crystals. Using the automated habit classification algorithm by *Um and McFarquhar* [2009], the crystals were divided into seven categories: columns, plates, bullet rosettes, budding bullet rosettes, small and large irregular crystals, and spherical particles. The CPI was only used to identify the shape of large ice crystals because the blurring of images due to diffraction effects renders the shape classification of small ice crystals unreliable [*Ulanowski et al.*, 2004]. We thus consider the shapes of small ice crystals to be unknown and assess their impact on radiation by using different shape models. To maximize the impact, all small ice crystals are assumed to have the same shape. The shape models considered here are Gaussian random spheres [*Nousiainen and McFarquhar*, 2004], droxtals [*Yang et al.*, 2003], and Chebyshev particles [*McFarquhar et al.*, 2002]. The Gaussian random sphere, introduced by *Muinonen et al.* [1996], is a stochastic shape model where a sphere is deformed statistically using a spherical harmonics expansion. To ensure that the radii are positive, the expansion is applied to the logarithm of radius. Single model shapes are generated by randomizing the weights of the spherical harmonics expansion using statistics specified by the covariance function of radius. The Chebyshev shapes are obtained by introducing a deterministic perturbation in a form of a Chebyshev series to a circle, and by rotating the obtained perturbed circle to obtain the three-dimensional shape. The amplitude of the perturbation must be sufficiently small so that the radius of the perturbed sphere is always positive. Droxtals have 20 faces (12 isosceles trapezoid faces, six rectangular faces in the center, and a bottom and top hexagonal face) and its geometry is defined in terms of the radius of the circumscribing sphere touched by all the droxtal vertices and two angular parameters [*Yang et al.*, 2003]. The three shape models considered here are illustrated in the work of *Um and McFarquhar* [2011, Figures 6–8].

[11] The mass content can be computed from the size and shape distributions by making assumptions about how the mass or effective density of particles varies with maximum dimension and area ratio. Different techniques for computing mass from the 2DC size distributions were compared against a mass content that was directly measured by a counterflow virtual impactor (CVI). The CVI provides bulk measures of the total water content, or equivalently ice water content in cirrus clouds, by evaporating particles with $D >$ 5 μm in dry air and measuring the resulting water vapor with a tunable diode laser absorption hygrometer [*Twohy et al.*, 2003]. The CVIs are estimated to have an accuracy of approximately 15% [*McFarquhar et al.*, 2007], much less than the differences between various techniques used to calculate mass from the size distributions. Thus, the CVI IWC is assumed to represent the base measure of mass in this study.

[12] Four different techniques were used to estimate mass from crystal sizes with $D > 120$ μm. In the first three, the habit is determined from the maximum dimension and area ratio of the crystal [*McFarquhar and Heymsfield*, 1996], and the mass is estimated using habit-dependent relationships as a function of size or both size and area ratio. The first mass calculation technique is based on the idealized crystals in the work of *Yang et al.* [2000], the second on the habit identification and mass relationships by *McFarquhar and Heymsfield* [1997], and the third on the *Heymsfield et al.* [2002] relationships. In the fourth, habits derived from the CPI are applied to the size distributions measured by the 2DC. Because of the limited sample volume of the CPI compared to that of the 2DC, an averaging time of 60 s is required to get a statistically significant habit distribution. These 60 s habit classifications are applied to all 10 s average size distributions derived from the 2DC covering this 60 s period. Figure 4 shows that the CPI/2DC habit identification/mass calculation scheme provides the best agreement with the CVI IWC when all measurements in cirrus from the Cloud IOP are used. Contributions from small crystals with $D < 120$ μm were not included in Figure 4. However, Figure 5 shows that even if the FSSP and 1DC are assumed to accurately measure small ice crystals, these crystals contribute less than 20% to the total IWC. Following *McFarquhar et al.* [2003], this represents an upper bound for the mass contribution of the small ice particles. Thus, despite the uncertainty in estimating the number distribution function *N(D)* for $D < 120$ μm, the 2DC/CPI size/habit distributions provide a mass estimate most consistent with the CVI data, and hence are henceforth used to characterize crystals with $D > 120$ μm.

[13] Figure 6 shows the size-shape distributions $N(D,s)$ measured by the FSSP, 1DC, 2DC, and CPI for four different altitude ranges for profile B. The shadings represent the fraction of different habits for the varying size ranges identified from the automated habit analysis. According to the automated habit analysis, bullet rosettes (*ros*) make fractional contributions of about 50% to the measured number of largest particles ($D > 500$ μm) near the upper portions of the cloud, whereas their contribution is smaller near the cloud base, with almost all very large crystals classified as big irregulars (*bir*) near the cloud base. Many of these big irregulars are actually aggregates of bullet rosettes, consistent with *Heymsfield et al.*'s [2002] observation that cirrus on this day was dominated by bullet rosettes. In addition, larger crystals were more frequent near the cloud base, with crystal mean diameters increasing from approximately 150 μm near the cloud top to around 400 μm near the cloud base. In Figure 6 it is seen that a small portion of crystals with $50 < D < 100$ μm were classified as shapes other than small irregular (*sir*) or spherical (*sph*); however, because the percentage of the crystals that were budding bullet rosettes (*bud*), bullet rosettes (*ros*), or columns (*col*) was small, the sensitivity studies simply assumed that all of the small crystals were quasi-spherical.

[14] Because the shapes and concentrations of small ice crystals are largely uncertain, five alternate representations were used to characterize the number distribution functions, *N(D)*, for small ice crystals with maximum dimension $D <$ 120 μm: *N(D)* measured by the FSSP and 1DC data with shapes represented by (1) droxtals; (2) Gaussian random spheres; (3) Chebyshev particles; (4) $N(D) = 0$ for $D < 50$ μm and *N(D)* from the 1DC for $D \geq 50$ μm with shapes assumed to be Gaussian random spheres; and (5) no small crystals with $D < 120$ μm. The size-shape distributions based on these different assumptions about small ice crystals are described in Table 2. These size-shape distributions

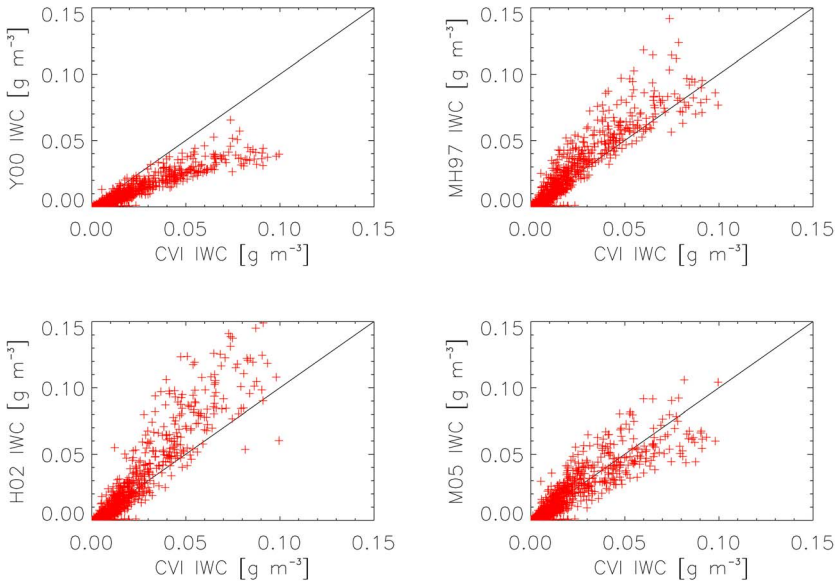

Figure 4. Comparison of bulk mass content measured by CVI against that estimated from 2DC size distributions or CPI/2DC size/habit distributions and a variety of mass-diameter or mass-diameter-area ratio relationships. Y00, masses from *Yang et al.* [2000] idealized crystals; MH97, habit identification and mass relationships of *McFarquhar and Heymsfield* [1997]; H02, *Heymsfield et al.* [2002] mass relationships; and M05, *McFarquhar et al.* [2005] habit identification scheme using CPI data and 2DC size distributions.

represent plausible descriptions of the sizes and shapes of ice crystals that occurred in the midlatitude cirrus sampled on this day. *Um and McFarquhar* [2011] show that the detailed shapes of small ice crystals cannot be identified using the CPI because its image resolution is not sufficient to resolve the fine structure of the crystals. That is the reason for considering three different shape models for these small crystals. The physical basis for considering the size-shape distribution with no small crystals is that their concentrations are quite uncertain. *Field et al.* [2006] and *McFarquhar et al.* [2007, 2011] have shown that the majority of crystals measured by forward scattering probes may be artifacts produced by the shattering of large ice crystals on probe inlets. Thus, the simulations with no small crystals represent a lower bound on their concentration, whereas the simulations using the measured concentrations represent an upper bound. In reality, there is probably some mixture of the assumed shapes and concentrations between the extremes, so that the real size-shape distributions should fall somewhere between these extremes.

2.2. Radiation Measurements

[15] Ground-based radiation measurements were used as reference for the shortwave radiative transfer simulations based on the measured microphysical and thermodynamic profiles. The shortwave ($300 < \lambda < 2800$ nm, where λ is the wavelength) radiation measurements and surface albedo, as well as the solar zenith angles were obtained from the best estimate flux value-added procedure [*Shi and Long*, 2002]. This product automatically determines the best estimate of direct and diffuse upward and downward radiative fluxes from colocated normal incidence pyrheliometers, shaded pyranometers, and shaded pyrgeometers at the SGP central facility. Due to the technique used to measure the direct radiation, it can also include some circumsolar irradiance coming from the direction of the sun, within a radius of about 3° (http://www.eppleylab.com/PrdNormIncPyrhelmtr.htm).

3. Optical Properties

[16] The single-scattering properties (i.e., extinction cross section C_{ext}, single-scattering albedo ω, and asymmetry parameter g) of individual ice crystals are obtained from state-of-the-art libraries of single-scattering properties of idealized ice crystals. The size, shape, and wavelength-dependent single-scattering properties of droxtals, Chebyshev particles, and large ideal ice crystals (column, plate,

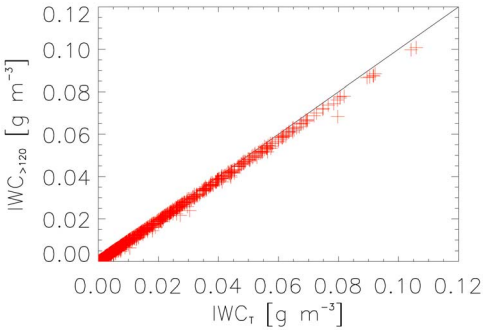

Figure 5. Mass estimated from 2DC/CPI size/habit distributions ($IWC_{>120}$) against mass estimated from 2DC/CPI plus that using the 1DC and FSSP size distributions (IWC_T). The close agreement between $IWC_{>120}$ and IWC_T indicates that small crystals from the 1DC and FSSP contribute minimally to the total mass.

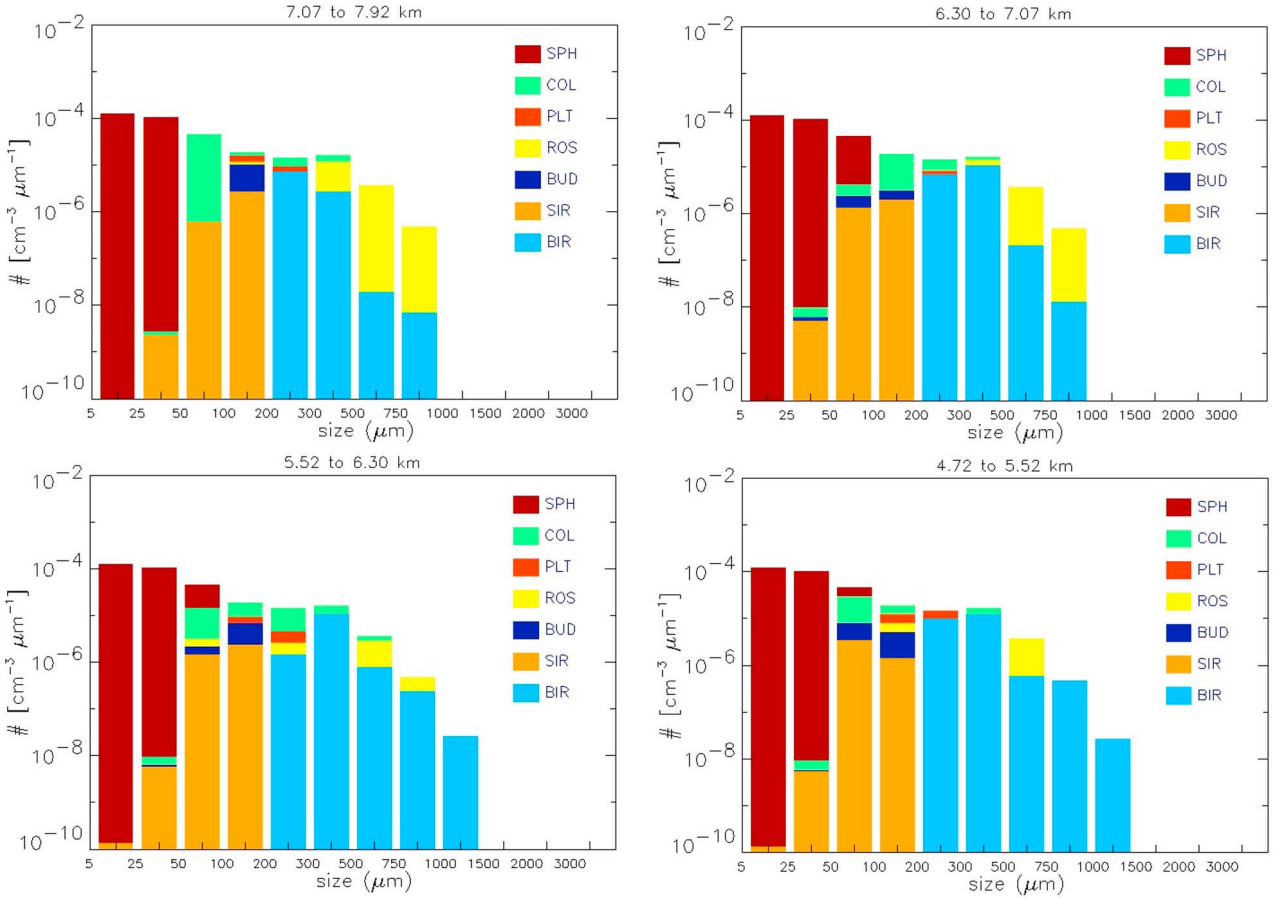

Figure 6. Size-shape distributions *N(D,s)* at four different altitude ranges of profile B measured by the FSSP, 1DC, and 2DC. The height of each column indicates the total number of particles in a given size range (logarithmic scale on the *y* axis). The fraction of particles of each habit is shown with different colors (in a linear scale). The habit categories used are sphere (*sph*), column (*col*), plate (*plt*), bullet rosette (*ros*), budding bullet rosette (*bud*), and small (SIR) and big (BIR) irregulars.

bullet rosette, budding bullet rosette, spherical, and small and big irregular) have been provided by *Yang et al.* [2003], *McFarquhar et al.* [2002] and *Yang et al.* [2000], respectively. Corresponding calculations for Gaussian random-sphere ice crystals with $D < 120$ μm have been conducted by T. Nousiainen (unpublished data). These single-scattering properties of ice crystals are given for 56 wavelength bands covering the range from 200 nm to 5000 nm. The previously introduced five alternative size-shape distributions are combined with these single-scattering properties of individual crystals to obtain vertical profiles of ensemble-averaged optical properties: volume-extinction coefficient (K_{ext}), single-scattering albedo, and asymmetry parameter. Following *Macke et al.* [1998], these properties are obtained here by integration over 65 sizes and eight shapes of ice crystals:

$$K_{\mathrm{ext}} = \sum_{i=1}^{65} \sum_{j=1}^{8} C_{\mathrm{ext}}(D_{\mathrm{i}}, s_{\mathrm{j}}) N(D_{\mathrm{i}}, s_{\mathrm{j}}), \tag{1}$$

$$g = \frac{\sum_{i=1}^{65} \sum_{j=1}^{8} g(D_i, s_j)\omega(D_i, s_j) C_{\mathrm{ext}}(D_i, s_j) N(D_i, s_j)}{\sum_{i=1}^{65} \sum_{j=1}^{8} \omega(D_i, s_j) C_{\mathrm{ext}}(D_i, s_j) N(D_i, s_j)}, \tag{2}$$

Table 2. The Size-Shape Distributions

Label	$D \geq 120$ (μm)	$50 \leq D < 120$ (μm)	$5 \leq D < 50$ (μm)
Large+droxtal	CPI-habits	droxtal	droxtal
Large+grs	CPI-habits	Gaussian random sphere	Gaussian random sphere
Large+Chebyshev	CPI-habits	Chebyshev	Chebyshev
Large+grs50	CPI-habits	Gaussian random sphere	-
Large+nosmall	CPI-habits	-	-

Table 3. The Wavelength Bands Used in the Radiative Transfer Simulations[a]

	1	2	3	4	5	6	7	8	9	10	11	12	13	14	15	16	17
Lower limit	300	372	450	513	600	700	791	844	889	975	1046	1194	1516	1614	1965	2153	2275
Mean	342	411	481	556	650	746	818	867	932	1010	1120	1355	1565	1789	2059	2214	2639
Upper limit	372	450	513	600	700	791	844	889	975	1046	1194	1516	1614	1965	2153	2275	2800

[a]Unit is nm.

$$\omega = \frac{\sum_{i=1}^{65}\sum_{j=1}^{8} \omega\left(D_i, s_j\right) C_{\text{ext}}\left(D_i, s_j\right) N\left(D_i, s_j\right)}{\sum_{i=1}^{65}\sum_{j=1}^{8} C_{\text{ext}}\left(D_i, s_j\right) N\left(D_i, s_j\right)}, \tag{3}$$

where $N(D_i,s_j)$ is the concentration of the crystals in a bin centered at size D_i with shape s_j. Note that C_{ext} is a product of extinction efficiency Q_{ext} and the cross-sectional area, and Q_{ext} is very close to 2.0 for most crystals in the distributions. Thus, C_{ext} and K_{ext} correlate well with cross-sectional area.

[17] The ensemble-averaged optical properties for the original 56 wavelength bands were averaged for 17 broader bands (Table 3) used in the radiative transfer simulations by weighting the optical properties for the original wavelengths by the corresponding top-of-the-atmosphere solar irradiance. Again, the single-scattering albedo was also weighted by K_{ext} and the asymmetry parameter by ω and K_{ext}.

[18] Vertical profiles of g, ω, and K_{ext} obtained from the flight profiles A and B by using different assumptions about the size and shape of small ice crystals are shown in Figure 7 for wavelength bands λ_{mean} = 556 nm and λ_{mean} = 2639 nm. The single-scattering albedo at λ_{mean} = 556 nm is very close to unity ($\omega > 0.9999$) and is therefore not shown. Profiles A and B show distinct differences in the volume extinction coefficient, with the maximum values being substantially larger for profile A. There is also a slight tendency for the asymmetry parameter to be larger for profile A than profile B, while the values of ω at λ_{mean} = 2639 nm are slightly higher for profile B. This is consistent with the presence of larger

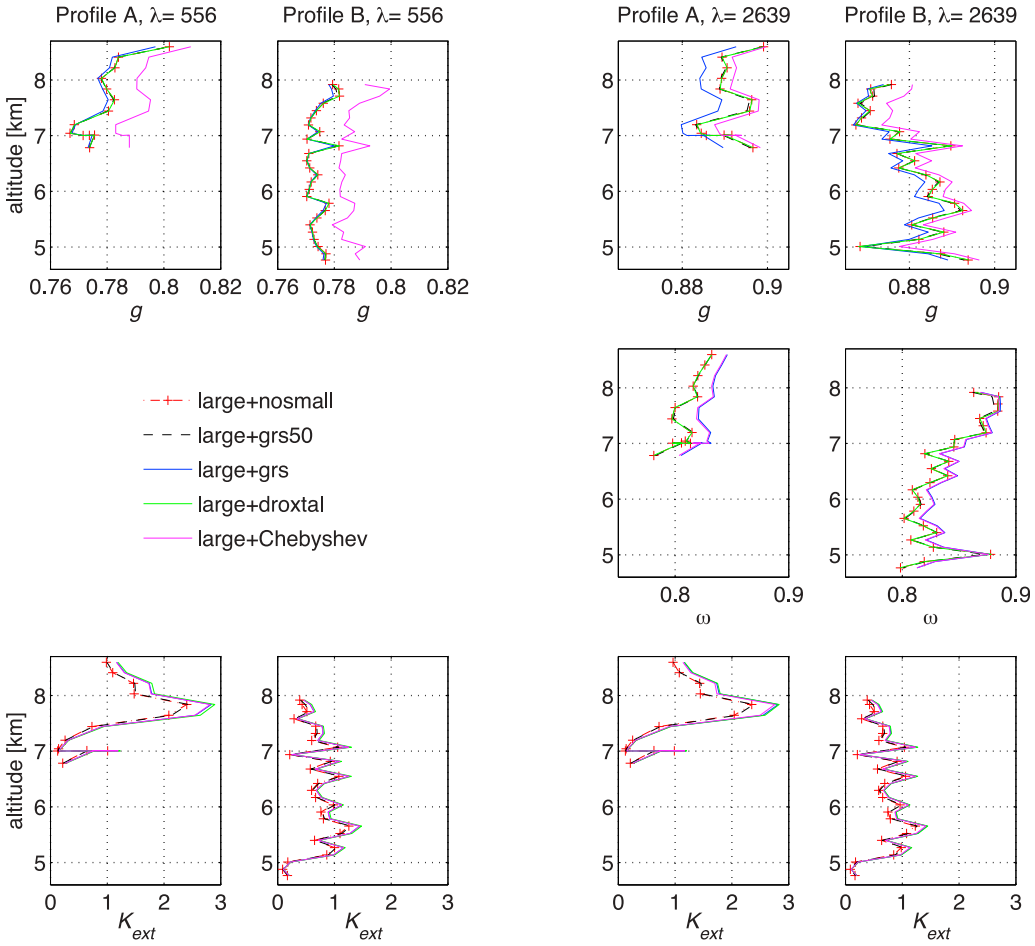

Figure 7. Vertical profiles of ensemble-averaged g, ω, and K_{ext} (1/km) at wavelengths (left) 556 nm and (right) 2639 nm computed from the different size-shape distributions of profiles A and B. The shoulder around 7 km altitude in profile A corresponds to a short horizontal path in the flight profile. The single-scattering albedos at λ_{mean} = 556 nm are not shown as they are very close to unity ($\omega > 0.9999$).

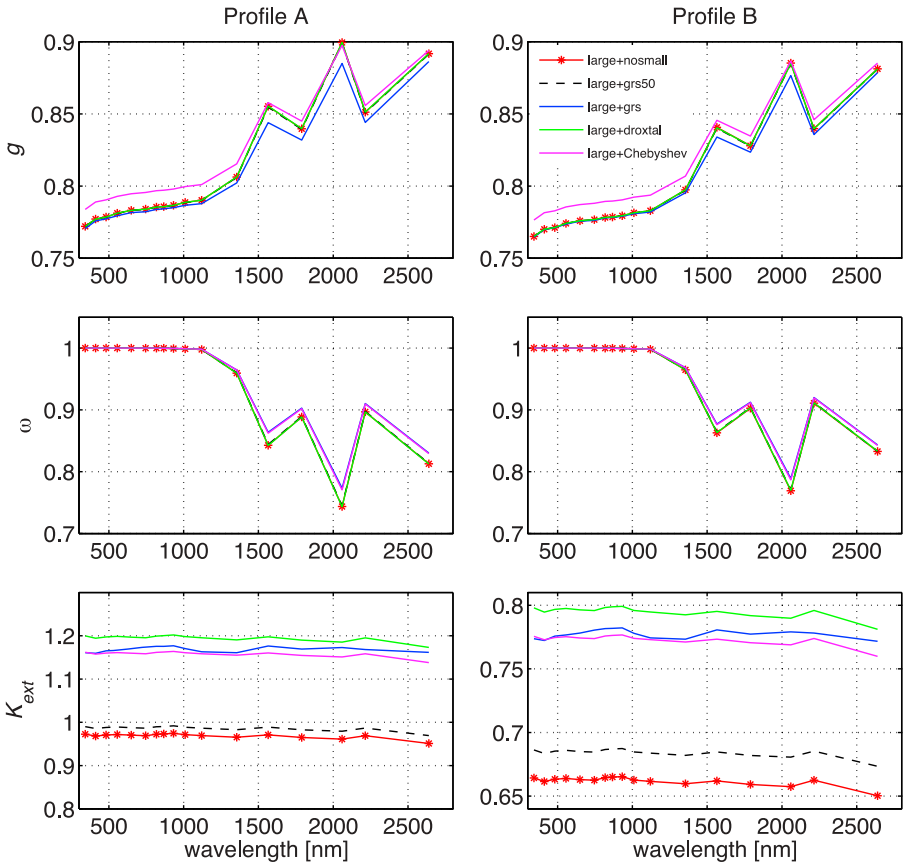

Figure 8. Vertically integrated values of ensemble-averaged g, ω, and K_{ext} (1/km) for different size-shape distributions of profiles (left) A and (right) B as a function of wavelength.

ice crystals in profile A (not shown). Not surprisingly, the distributions that include crystals with $5 < D < 50$ μm (*large+droxtal*, *large+grs* and *large+Chebyshev* distributions) yield larger K_{ext} than *large+nosmall* and *large+grs50* distributions. As mentioned earlier, the concentrations of these small ice crystals are highly uncertain. The spread in lines in Figure 7 illustrates how this uncertainty affects the optical properties. It is noted that the wavelength dependence of the alternative size-shape distributions is slightly different. To distinguish better how the use of different size-shape distributions affects the optical properties and how the effect depends on wavelength, vertically integrated g, ω, and K_{ext} are shown as a function of wavelength in Figure 8.

[19] Contrary to g and ω, the volume extinction coefficient does not depend strongly on wavelength and thus the differences between size-shape distributions are nearly constant (Figure 8). This is because most crystals are much larger than wavelength and thus Q_{ext} is almost independent of λ. It is also noted that the use of *large+nosmall* and *large+grs50* distributions produce almost identical profiles of g, ω, and K_{ext}, showing that particles in the range from 50 to 120 μm do not contribute much to the optical properties on this day. Because these concentrations are likely overestimates due to impacts of shattering [*Korolev et al.*, 2011] their minimal contributions to the optical properties suggests our approach for deriving these properties is still robust. Thus, even though the concentrations of particles in this size range are highly uncertain, this does not translate into a large uncertainty in the calculated optical properties because their fractional contribution to the total surface area, and hence the total extinction, is quite small. Particles with $D < 50$ μm, however, can contribute significantly, and thus uncertainties in their concentrations impact K_{ext}, g, and ω depending on the model used to represent small crystals. When the whole size distribution of crystals is included, the largest K_{ext} are obtained with the *large+droxtal* distribution and the smallest with the *large+Chebyshev* distribution. These differences are, however, small. The differences are largely due to different area ratios for different shape models: as shown by *Um and McFarquhar* [2011], K_{ext} for the small crystals varies between the assumed shapes.

[20] The increase in g and decrease in ω with increasing wavelength is due to the increased absorption at longer wavelengths. For both profiles, the *large+droxtal* distribution gives similar results for the asymmetry parameter as those distributions that do not include particles with $D <$ 50 μm, whereas at short wavelengths the *large+Chebyshev* and at longer wavelengths the *large+grs* distributions differs notably from the g of the *large+nosmall* distributions. At each wavelength, the *large+grs* distribution yields smaller and *large+Chebyshev* distribution larger (except at 2059 nm) values of g than the *large+nosmall* distribution. The single-scattering albedo exceeds 0.99 at wavelengths bands with $\lambda_{mean} \leq 1120$ nm for both profiles, regardless of the size-shape distribution. At wavelengths larger than 1120 nm, ω is larger for the *large+Chebyshev* and *large+grs*

Table 4. Cloud Optical Thickness at λ_{mean} = 556 nm for Both Profiles Based on the Different Size-Shape Distributions

Profile	*large+nosmall*	*large+grs50*	*large+Chebyshev*	*large+grs*	*large+droxtal*
A	2.16	2.20	2.59	2.60	2.67
B	2.18	2.25	2.54	2.54	2.61

distributions than for the other distributions. The larger g and ω for the Chebyshev approximation followed by the Gaussian random sphere and droxtal approximations is consistent with the analysis by *Um and McFarquhar* [2011] that compared the single-scattering properties of different small crystal models.

[21] The optical thickness for each layer (τ_i) is also needed as input for the radiative transfer simulations. Values of τ_i are calculated from the vertical profiles of K_{ext} by

$$\tau_i(\lambda) = K_{ext,i}(\lambda)\,\Delta z_i, \quad (4)$$

where Δz_i is the thickness of the layer i. The layer bounds are defined by the change of flight altitude during 1 min of the flight, except for the lowest layer of profile B which covers only 40 s. The cloud optical thickness, τ, at λ_{mean} = 556 nm integrated over the entire cloud depth is shown in Table 4 for all five size-shape distributions of both profiles. The smallest optical thicknesses are, of course, obtained by ignoring small particles (the *large+nosmall* distributions). The Chebyshev and Gaussian random-sphere shape approximations of small ice crystals lead to very similar τ with differences smaller than 0.01 for both profiles. The droxtal approximation yields slightly larger values, as expected from the profiles of K_{ext} shown in Figures 7 and 8. Based on Table 4, the τ values at λ = 556 nm are very similar for both profiles (within 0.06 for each size-shape distribution). This occurs because profile A covered a shorter vertical distance but had optically denser layers than profile B. The contribution to cloud optical depth of particles with $50 < D < 120$ μm is very small (0.04 for profile A and 0.07 for profile B) as compared with that of larger particles (2.16 and 2.18 for profiles A and B, respectively) and of the smallest particles, which varies between 0.39 and 0.47 for profile A and from 0.29 to 0.36 for profile B depending on the assumed shape. Based on Table 4 it is evident that small crystals ($5 < D < 50$ μm) can make significant contributions to the cloud optical thickness if their maximum possible concentrations are assumed. Depending on the shape approximation (Chebyshev, Gaussian random sphere, or droxtal) this contribution is 17.6%, 18.2% or 21.4% of the τ(556) of *large+grs50* in case of profile A; for profile B the corresponding contributions are 13.0%, 13.3% or 16.4%.

4. Radiative Transfer Model

[22] The libRadtran radiative transfer package [*Mayer and Kylling*, 2005] was used for simulating the SW radiative effect of the cirrus cloud. The radiative transfer equation was solved using the DIScrete Ordinate Radiative Transfer model (DISORT2) [*Stamnes et al.*, 1988] with 16 streams for angular discretization of the radiance field. Gaseous absorption and scattering coefficients in the UV and visible regions between λ = 300 nm and λ = 791 nm were specified at 1 nm spectral resolution, while for λ > 791 nm, the correlated k distribution model by *Kato et al.* [1999] was used for gaseous absorption. Cloud optical properties, i.e., the values of τ, ω, and g for each layer, were specified for 17 wavelength bands (Table 3). The scattering phase function of cloud particles was derived from g assuming the parametrization by *Henyey and Greenstein* [1941].

[23] Vertical profiles of pressure, temperature, and humidity up to an altitude of about 25 km were obtained from the central facility radiosonde soundings on 13 March 2000. The "U.S. standard" atmospheric profile [*Anderson et al.*, 1986] was used to extend these profiles up to the top of the atmosphere as well as to provide profiles of O_3, O_2, CO_2 and NO_2 throughout the atmosphere. The sounding released at 17:29 GMT was used to create the model atmosphere for profile A and the 20:30 sounding for profile B. The cirrus cloud was described using the layer values of τ, ω, and g obtained from the five size-shape distributions of profiles A and B. An overcast, plane-parallel, horizontally homogeneous cloud was assumed. Based on *Buschmann et al.* [2002], the plane parallel approximation for relatively homogeneous (e.g., nonconvective) midlatitude cirrus most likely does not induce flux errors larger than 10%. Thus, when calculating the temporal evolution of the modeled fluxes, the cloud was assumed horizontally homogeneous and only the solar zenith angle (θ_0) was varied. Table 5 shows how θ_0 varies with the time of day from 18 to 23 GMT. A wavelength-independent surface albedo of 0.2 was used. This value is a median value between 18 and 23 GMT of the surface albedo obtained from the best estimate flux value-added procedure. Finally, in the absence of aerosol information, aerosols were not included in the calculations.

5. Results and Discussion

5.1. Impact of Assumptions About Small Ice Crystals

[24] The output of the libRadtran radiative transfer model includes the direct (F_{dir}), diffuse (F_{diff}) and total ($F^{\downarrow} = F_{dir} + F_{diff}$) downward fluxes at the surface, and the upward flux at the top of the atmosphere ($F^{\uparrow}$). From these fluxes the SW

Table 5. Solar Zenith Angles at the SGP CF From 18 to 23 GMT for 13 March 2000

	GMT[a] (h)										
	18:00	18:30	19:00	19:30	20:00	20:30	21:00	21:30	22:00	22:30	23:00
θ_0(°)	40.24	39.24	39.46	40.90	43.43	46.86	51.01	55.71	60.82	66.24	71.87

[a]Geomagnetic time.

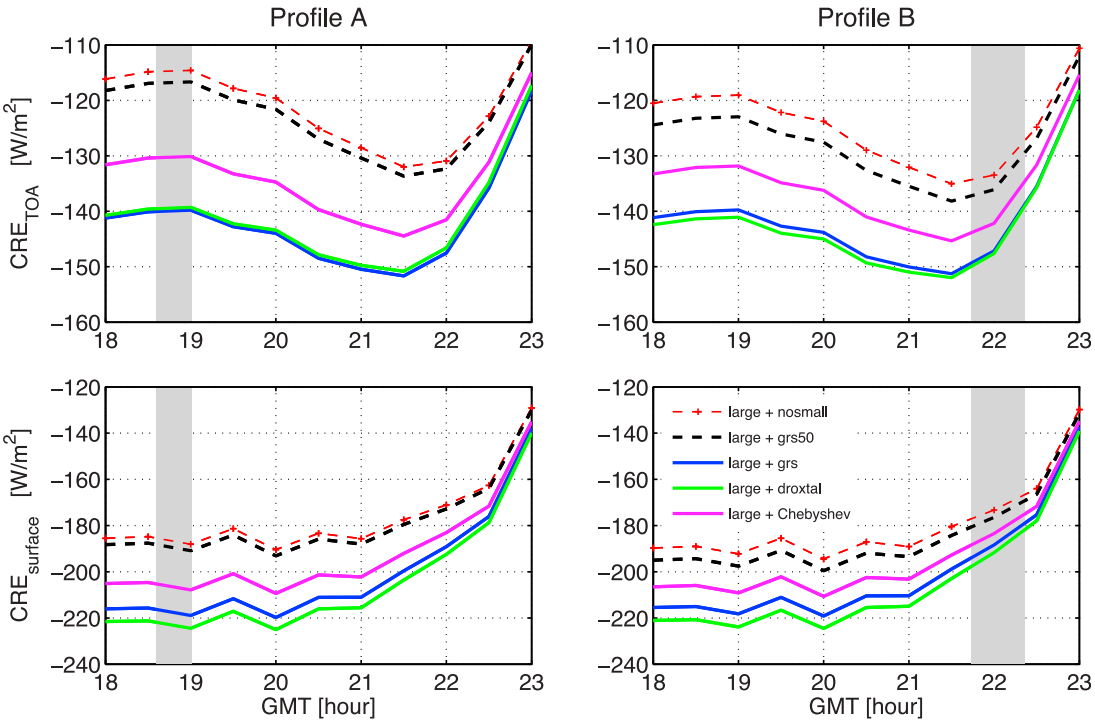

Figure 9. The SW cloud radiative effects at the TOA (CRE_{TOA}) and at the surface ($CRE_{surface}$) based on alternative size-shape distributions of profiles A and B. The CREs are shown as a function of time, and the gray bars represent the time of the flight profile ±6 min.

cloud radiative effects both at the TOA (CRE_{TOA}) and at the surface ($CRE_{surface}$) were determined:

$$CRE_{TOA} = F^{\uparrow}_{\text{clear sky}} - F^{\uparrow}_{\text{cloudy sky}} \quad (5)$$

and

$$CRE_{surface} = F^{\downarrow}_{\text{cloudy sky}} - F^{\downarrow}_{\text{clear sky}}. \quad (6)$$

The SW cloud radiative effects (CRE_{TOA} and $CRE_{surface}$) based on the profiles A and B are shown in Figure 9 as a function of time. CREs and their sensitivities to the size-shape distribution depend strongly on the solar zenith angle. CREs become weaker in the evening with decreasing solar elevation, but CRE_{TOA} also has a local minimum during midday (about 18:30 GMT). During the time period from 18 to 23 GMT, CREs based on profiles A and B differ at most by 7 W/m^2, the exact values depending on the assumed size-shape distribution. Crystals with $5 < D < 50$ μm have notably larger impact on CRE than crystals with $50 < D < 120$ μm, consistent with their impact on τ reported in section 3. As mentioned in section 2.1, the concentrations for $D < 50$ μm may be greatly overestimated due to shattering. Hence, the results do not necessarily indicate a large CRE of small crystals, but rather the need for reliable and accurate measurements of small crystal concentrations.

[25] The cloud radiative effect is also sensitive to the shape of small ice crystals. Even though CRE_{TOA} based on the Gaussian random spheres and droxtals are very similar (<1.5 W/m^2 difference), the use of Chebyshev particles yields larger differences (from 2 to 10 W/m^2). The same is also true for $CRE_{surface}$. Since ω and K_{ext} of *large+Chebyshev* and *large+grs* distributions are closer to each other than those of the *large+grs* and *large+droxtal* distributions, the large difference in CRE between the *large+Chebyshev* and *large+grs* distributions is undoubtedly due to the larger asymmetry parameter of Chebyshev particles at short wavelengths where most of the solar radiation energy is. The strongest $CRE_{surface}$ is obtained with the *large+droxtal* distribution, presumably because droxtals have the largest K_{ext} of all the size-shape distributions used.

5.2. Comparison With Radiative Flux Observations

[26] The modeled surface SW fluxes based on different size-shape distributions are also compared against measured fluxes at the SGP central facility. The comparison is not trivial, however, because the measured direct flux contains radiation scattered into the near-forward direction, while in computations all scattered radiation is accounted for in the diffuse flux. To correct for this, the amount of scattered radiation in the measured direct flux must be added to the computed direct fluxes and removed from the computed diffuse fluxes. To quantify this amount, the direct fluxes were computed in each case with two different optical thicknesses (the actual optical thickness, τ, of the cloud and τ multiplied by 0.48) as discussed in Appendix A. After this correction, computed and measured fluxes could be directly compared. Hereafter, all modeled direct and diffuse fluxes include this correction.

[27] The comparison of modeled and measured fluxes is shown in Figure 10. For most of the time, the differences between the modeled and observed fluxes are much larger than those associated with the uncertainties related to small ice crystals. During profiles A and B (±6 min), the modeled

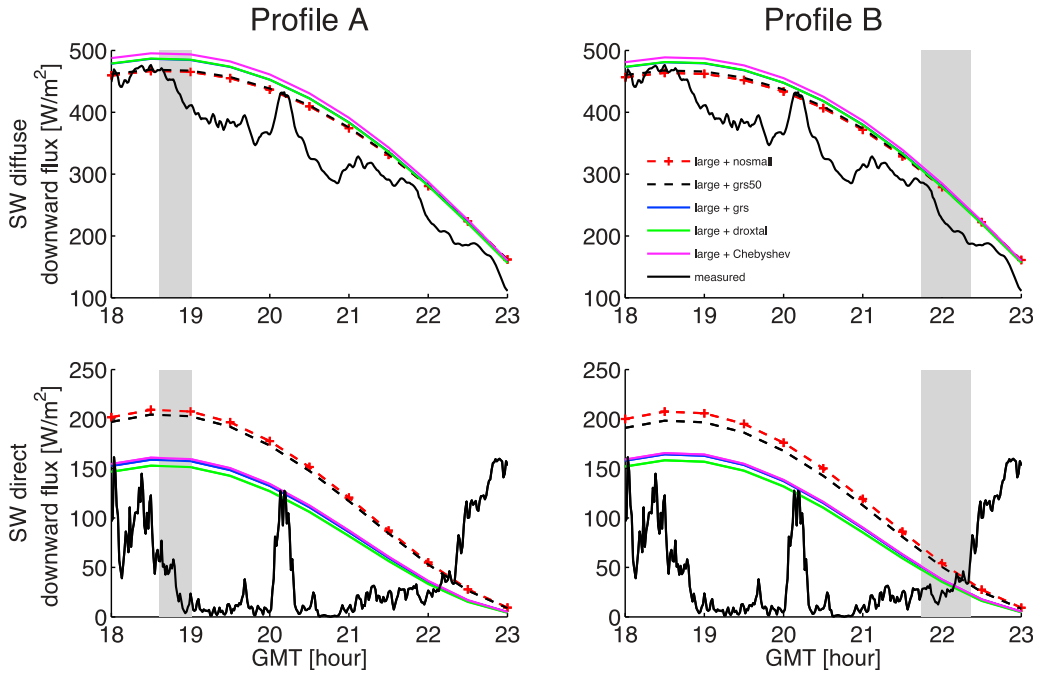

Figure 10. The modeled direct and diffuse downward fluxes at the surface computed for the different size-shape distributions of profiles A and B compared against measurements. The gray bars represent the time of the flight profile ±6 min.

fluxes tend to overestimate the measured fluxes, with average differences being 144 W/m^2 and 12 W/m^2 for the direct and 37 W/m^2 and 44 W/m^2 for the diffuse flux, respectively. The differences between fluxes produced by varying the size-shape distributions are less than 50 W/m^2 for direct radiation and less than 25 W/m^2 for diffuse flux. The large fluctuations of measured direct flux during the profiles A and B imply that the cloud cover over the central facility was not homogeneous during the time of the flight profiles. It is possible that three-dimensional radiative effects associated with cloud inhomogeneity might be the reason for the poor agreement between the modeled and measured fluxes. In addition, there are several other factors that could have contributed to these discrepancies, including inaccurate and uncertain observations of the size and shape of ice crystals, knowledge of the scattering properties of ice crystals, and the spatial separation between the locations of the flight and ground measurements.

[28] However, it was possible to greatly reduce the gap between the observed and modeled fluxes by accounting for only two of these factors. First, the cloud optical thickness evolves with time and is not well constrained by the in situ data. It also appears that a small portion of the top and possibly the bottom of the cloud was missed on the ramped horizontal ascent for profile A based on the MMCR image and flight notes. Second, *Ulanowski et al.* [2010] recently showed that most ice crystals might have rough surfaces. Morphological features such as surface roughness or internal inclusions can give rise to a more isotropic distribution of the scattered radiation, thus reducing g [e.g., *Macke et al.*, 1996; *Kahnert et al.*, 2008; *Nousiainen et al.*, 2011], which in turn affect the radiative fluxes. The impacts of these factors are discussed in section 5.3.

5.3. Sensitivity Tests

[29] To investigate the effect of varying cloud optical thickness, two alternate formulations of optical thickness derived from surface measurements collected at the ARM CF were used. First, the in situ measured $\tau_i(\lambda)$ (hereafter, $\tau_{\text{in situ}}(\lambda)$) were scaled so that they match the MMCR radar τ values at $\lambda = 500$ nm retrieved following *Mace et al.* [2006]. These τ are denoted as τ_{radar}. Second, τ was derived by matching the computed and measured direct radiation. To do so, $\tau_{\text{in situ}}(\lambda)$ was replaced by

$$\tau_{\text{i, dirfit}}(\lambda, t) = \tau_{\text{i, in situ}}(\lambda)x(t), \tag{7}$$

where t is time and x is a wavelength-independent but time-dependent correction factor. It is estimated by applying Beer's law in the form

$$F_{\text{dir,obs}}(t) = F_{\text{dir,calc}}(t)\exp\left\{-\frac{0.48\,[x(t)-1]\,\tau_{556}}{\cos\theta_0(t)}\right\}, \tag{8}$$

where θ_0 is the solar zenith angle, $F_{\text{dir,obs}}$ is the observed direct flux, $F_{\text{dir,calc}}$ is the direct flux calculated using the $\tau_{\text{in situ}}$ and θ_0, and τ_{556} is the value of $\tau_{\text{in situ}}$ at $\lambda_{\text{mean}} = 556$ nm. The factor 0.48 is used to account for the fact that $F_{\text{dir,obs}}$ includes some scattered radiation (see Appendix A). This yields

$$x(t) = \frac{\cos\theta_0(t)}{0.48\tau_{556}}\ln\left(\frac{F_{\text{dir,calc}}}{F_{\text{dir,obs}}}\right) + 1. \tag{9}$$

Here, a 3 min temporal resolution, rather than the previously used 30 min temporal resolution, was adopted for the solar zenith angles. For the *large+grs* distribution of profile B, the values of x fluctuated between 0.13 and 3.90, leading to τ values (hereafter, τ_{dirfit}) between 0.33 and 9.92 at a

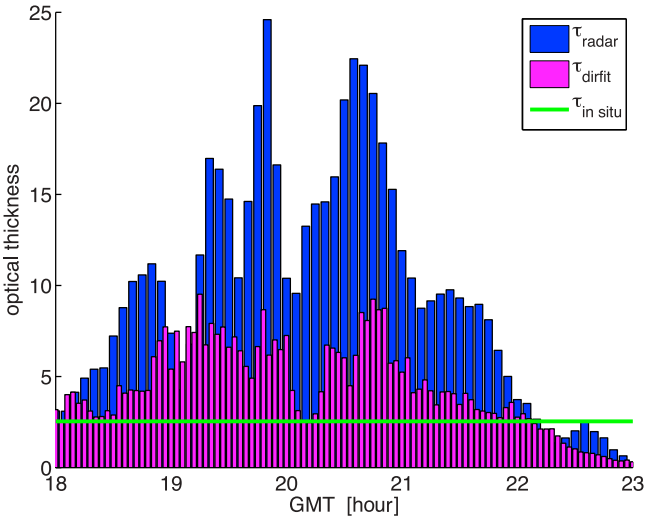

Figure 11. Optical thicknesses retrieved from MMCR radar data (τ_{radar}) [*Mace et al.*, 2006] and from measured direct radiation (τ_{dirfit}) shown together with that based on flight measurements ($\tau_{in\ situ}$).

wavelength of 556 nm, while the original τ (hereafter, $\tau_{in\ situ}$) was 2.54. The comparison of τ_{radar}, τ_{dirfit}, and $\tau_{in\ situ}$ at $\lambda_{mean} = 481$ nm is shown as a function of time in Figure 11. The values of τ_{radar} are notably larger than those of τ_{dirfit} or $\tau_{in\ situ}$, especially around 20:30 GMT.

[30] For simplicity and because of the similarity of the in situ profiles, the radiative transfer simulations for the sensitivity tests (τ_{radar}, τ_{dirfit}, and $\tau_{in\ situ}$) were conducted only using the optical properties (g and ω) of *large+grs* distribution of profile B. Physically, changing τ while keeping g and ω fixed correspond to the situation where the number concentration of the particles is changed, without changing the size and shape distributions The corresponding simulated direct, diffuse and total downward fluxes at the surface are compared to the measured fluxes in Figure 12. As expected, the measured and τ_{dirfit} direct fluxes are almost identical (minor difference of < 1.5 W/m^2 occur because the wavelength dependence of τ is neglected in (9)). In addition, the total fluxes based on τ_{dirfit} are very close to those measured, with an average difference of 19 W/m^2. During the profile B, the differences in total fluxes are relatively small between all cases. However, between the flights, the use of τ_{radar} values underestimates substantially the observed direct and diffuse fluxes.

[31] The other sensitivity test investigated the effect of ice crystal roughness on surface fluxes. Figure 12 shows how reducing g by 10% at all altitudes and wavelengths impacts the surface fluxes, with this case denoted by $\tau_{dirfit+90g}$. Interestingly, there is also observational evidence [*Stephens et al.*, 1990; *Kinne et al.*, 1992] that the bulk asymmetry parameter of crystals in ice clouds may be about 0.7, about 10% smaller than the values obtained here from ideal ice crystals. It was found that the measured diffuse and total fluxes are generally between those derived by using the cases τ_{dirfit} and $\tau_{dirfit+90g}$. Thus, it seems that a smaller reduction in g could give even better agreement between measured and modeled τ_{dirfit} fluxes. One notable exception is the time during profile B, when the simulated fluxes overestimate the measured diffuse flux. This could be associated with the unrepresentativeness of the direct-flux-derived τ due to large solar zenith angle: matching the direct flux constrains the optical thickness in the direction of the sun but not necessarily overhead.

6. Summary and Conclusion

[32] The shortwave radiative fluxes of a cirrus cloud were modeled using size-shape distributions of ice crystals obtained in situ by the UND Citation aircraft over ARM's Southern Great Plains measurement site during the March 2000 Cloud IOP. In this study data from one ramped horizontal ascent and one descent spiral of the UND Citation through a fairly horizontally homogeneous cirrus sampled on 13 March were used to assess the relative importance of assumptions about the size and shape distributions of small ice crystals ($D < 120$ μm) on radiative fluxes. The fluxes were also compared with measurements at the surface.

[33] Large crystals ($D > 120$ μm) were divided into seven habit classes (column, plate, bullet rosette, budding bullet rosette, spherical, and small and big irregular) using an automated habit classification algorithm based on the CPI

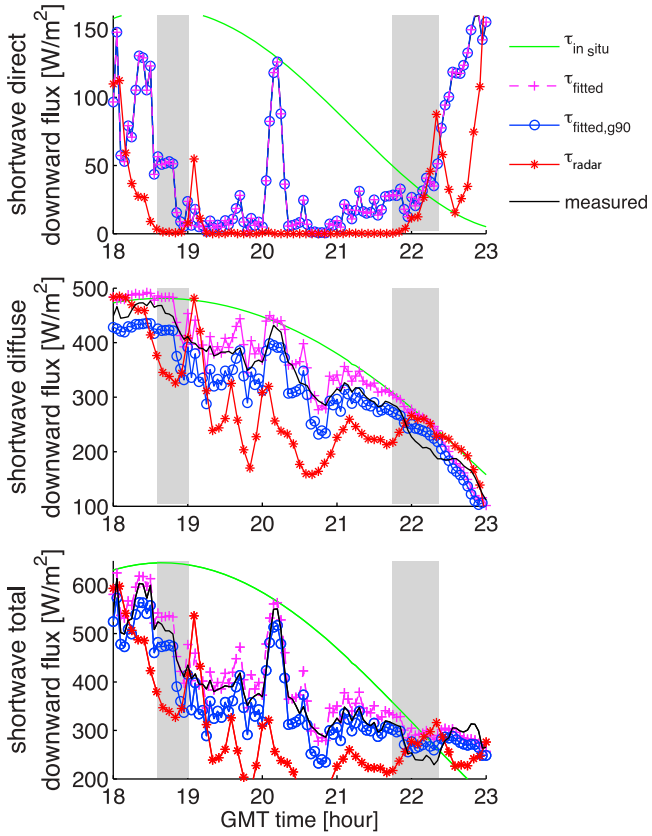

Figure 12. SW direct, diffuse, and total downward fluxes at the surface based on the sensitivity tests compared against measurements. Values of optical thicknesses of $\tau_{in\ stiu}$ (green) are based on flight measurements; values of optical thicknesses of τ_{dirfit} (magenta) and $\tau_{dirfir+90g}$ (blue) are retrieved from the direct radiation; and values of optical thicknesses of τ_{radar} (red) are retrieved from MMCR radar data [*Mace et al.*, 2006], respectively. The gray bars represent the time ranges of flight profiles A and B ±6 min.

measurements. Since the shape of small ice crystals ($D < 120$ μm) could not be reliably determined from the CPI images, three alternative shape models were used (Gaussian random spheres, droxtals, and Chebyshev particles). To account for the uncertainties associated with the concentrations of small ice crystals, two additional size-shape distributions with varying concentrations were considered. To obtain vertical profiles of ensemble-averaged optical properties (g, ω, and K_{ext}), the single-scattering properties of individual ice crystals were averaged over the size-shape distributions in each vertical layer.

[34] This study expounded upon past studies examining cloud radiative interactions by clearly quantifying the distinct impact of uncertainties in the concentration and shape of small ice crystals on radiative fluxes, hence offering interesting new insights into understanding the connection between particle morphology, cloud microphysics and cloud radiative effect. While the results for the Gaussian random-sphere or droxtal approximations deviate only slightly, the Chebyshev approximation leads to smaller cloud radiative effect both at the surface and TOA. The concentration of small ice crystals can also strongly influence the SW fluxes both at the surface and at the TOA. The crystals with $5 < D < 50$ μm had a stronger effect on the CREs than the crystals with $50 < D < 120$ μm. This is most likely a result of the artificial amplification of small crystal concentrations due to the possible shattering on probe tips.

[35] Even though the Cloud IOP provided detailed information about the size-shape distributions of ice crystals of the cloud studied, the modeled fluxes differed from the measurements by more than the observational uncertainties. The differences between simulated and observed fluxes were larger than those caused by uncertainties in the concentrations and shapes of small ice crystals. There are several simplifications made in the current study that could have contributed to this discrepancy. For example, the cloud was assumed to be horizontally homogeneous even though both the cloud radar data and the measured direct flux suggest that this is not the case. In addition, the horizontal noncoincidence of the flight profiles and the ground measurements was disregarded. According to *Buschmann et al.* [2002] the impact of cloud inhomogeneity on the radiative fluxes should be smaller than 10% for this type of cirrus. In our case, the discrepancies between the simulated and observed fluxes are, however, often larger than this, indicating that other factors are involved.

[36] To gain insight into the factors contributing to discrepancies between modeled and measured fluxes, additional sensitivity tests assessed the direct impact of changing τ and g on modeled fluxes. If the optical thickness was adjusted so that the measured and modeled direct fluxes matched, the modeled total flux fit the measurements well (mean difference less than 19 W/m^2). It was also found that reducing g by a factor of less than 10% could improve the agreement with measurements. A decrease in g could be associated to presence of surface roughness or air bubble inclusions or other nonidealities in the crystals, for example.

[37] Interestingly, g and ω were very similar for the two measured profiles. If this is a generic property of horizontally nearly homogeneous cirrus, it could prove useful. The observed radiative fluxes were reasonably well modeled over the whole day using vertical profiles of g and ω measured only in the evening and deriving the cloud optical thickness from the measured direct flux at the surface. Ideally, vertical profiles of in situ aircraft measurements coincident with scanning radar data should be used to derive three-dimensional cloud fields and corresponding single-scattering properties for use in studies investigating how different sizes and shapes of ice crystals affect radiative fluxes. A future study will use newer in situ measurements in combination with the radar data to derive vertical profiles of cloud parameters, from which surface fluxes can be calculated. This will not only improve the microphysical measurements, but also avoid problems with lack of colocation between microphysics profiles and surface fluxes. Further, more colocated measurements of in situ size and shape distributions with direct observations of scattering phase function should be obtained in the future in order to test the potential importance of surface roughness and inclusions on derived asymmetry parameters. All these steps will allow a test on the generality of the findings in this study.

Appendix A: Impact of Near-Forward Scattering on Measured Direct Fluxes

[38] It was noted in section 2.2 that the measures of "direct" solar radiation used in this work include circumsolar radiance coming from within ≈3° of the solar direction. The measured direct flux therefore includes not only the "true" direct flux (i.e., unscattered radiation) but also some diffuse (i.e., scattered) radiation. To make this distinction explicit, the notations F^{dir}_{true} and F^{dir}_{app} are hereafter used for the "true" and "apparent" (or measured) direct flux. To correct for the presence of scattered radiation in the measured direct flux in order to compare with the flux computed from DISORT2, it is necessary to study how F^{dir}_{app} depends on cloud optical thickness τ and solar zenith angle θ_0.

[39] For monochromatic radiation, the impact of a cloud layer on F^{dir}_{true} can be expressed as

$$F^{dir}_{true} = F^{dir}_{true,clear} \exp\left(\frac{-\tau}{\cos\ \theta_0}\right), \tag{A1}$$

where $F^{dir}_{true,clear}$ is the true direct flux in a cloud-free environment. *Shiobara and Asano* [1994] demonstrated that, to a good approximation, a similar expression can be applied to the computation of F^{dir}_{app}, provided that cloud optical thickness is replaced by an apparent optical thickness $\tau' = k\tau$:

$$F^{dir}_{app} = F^{dir}_{app,clear} \exp\left(\frac{-k\tau}{\cos\theta_0}\right), \tag{A2}$$

where $F^{dir}_{app,clear}$ is the apparent direct flux in clear-sky conditions, which in practice has a negligible difference from $F^{dir}_{dir,clear}$ for aerosol-free cases. The factor k can be computed using the single-scattering albedo ω and scattering phase function $P(\theta_s)$ of the cloud:

$$k = 1 - \omega \int_0^{\eta} P(\theta_s) \sin\theta_s d\theta_s, \tag{A3}$$

where η is the radius of the instrument field of view (in our case, $\eta = 3°$), θ_s is the scattering angle, and $P(\theta_s)$ is normalized so that its integral from 0° to 180° equals 1. This

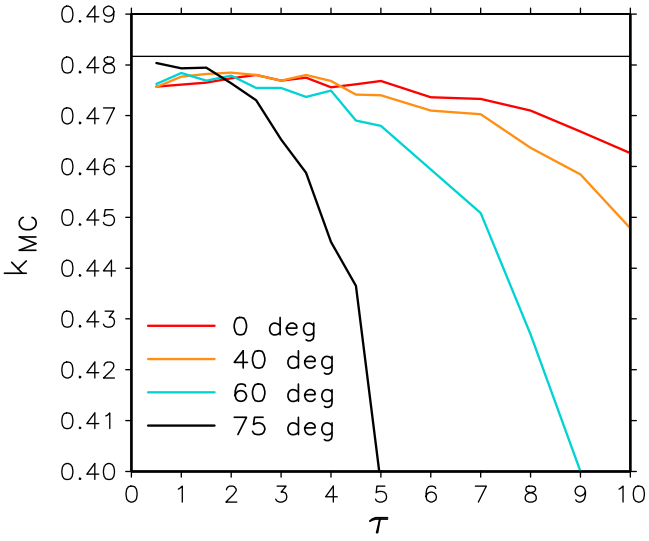

Figure A1. Ratio between apparent and true optical thickness (k_{MC}) derived from Monte Carlo results as a function of cloud optical thickness τ for four solar zenith angles: $\theta_0 = 0°$ (red), $\theta_0 = 40°$ (orange), $\theta_0 = 60°$ (blue), and $\theta_0 = 75°$ (black).

corresponds to the assumption that scattering at angles smaller than the instrument field of view does not contribute to the attenuation of apparent direct solar radiation, and can therefore be subtracted from the total optical depth.

[40] Strictly speaking, equations (A2) and (A3) are valid at the limit of optically thin clouds, that is, when multiple scattering can be neglected. In principle they only apply to monochromatic radiation, or for spectral intervals for which cloud optical properties can be considered constant. Here, we apply (A2) and (A3) to broadband shortwave radiation and compare the results to those obtained using a backward Monte Carlo model [*Pirazzini and Räisänen*, 2008]. For ice cloud single-scattering properties, including the phase function, average values for *large+droxtal* size-shape distribution of profile B are assumed. Averaged over the entire solar spectrum, the mean value of ω is 0.974, and the integral in (A3) for $\eta = 3°$ is 0.532, which reflects the strong dominance of near-forward scattering for particles much larger than wavelength. This yields a broadband average value of $k = 0.482$. Corresponding values computed for the four spectral bands used for cloud optics in the Monte Carlo model were $k = 0.470$ (for $\lambda = 0.25$–0.69 μm), $k = 0.480$ (for 0.69–1.19 μm), $k = 0.500$ (for 0.25–0.69 μm) and $k = 0.549$ (for 2.38–4.00 μm).

[41] Monte Carlo computations were carried out for 15 values of cloud optical thickness ranging from $\tau = 0.5$ to $\tau = 10$, for an ice cloud located between altitudes of 5 and 9 km. Two atmospheric profiles (midlatitude winter and midlatitude summer [*Anderson et al.*, 1986]) were considered. Because the results were very similar, only the midlatitude winter results are shown below. A surface albedo of 0.2 was assumed and four solar zenith angles were considered (0°, 40°, 60° and 75°), the intermediate values best representing the conditions for the 13 March 2000 case study. For each case, 25 million photons were used.

[42] By inverting (A2), the values of k can be derived from Monte Carlo (MC) calculations:

$$k_{MC} = -\frac{\cos\theta_0}{\tau}\ln\frac{F^{dir}_{app}(\tau)}{F^{dir}_{app,clear}}. \quad (A4)$$

It is seen from Figure A1 that for optically thin clouds, the values of k_{MC} are very close to the estimate $k = 0.482$ obtained using (A3). However, for optically thicker clouds, and particularly for large solar zenith angles, k_{MC} decreases somewhat. This occurs because multiple scattering of radiation originally scattered further away from the sun can add

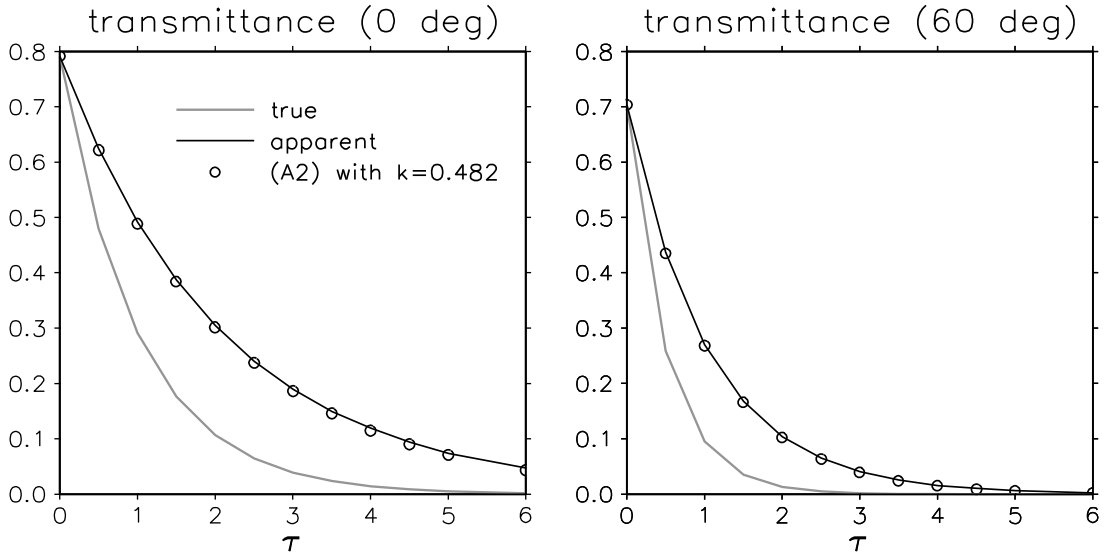

Figure A2. True direct broadband solar transmittance (gray line), apparent direct transmittance (black line), and the estimate of apparent direct transmittance derived from equation (A2) with $k = 0.482$ (open circles) as a function of cloud optical thickness, τ, for a solar zenith angle of (left) $\theta_0 = 0°$ and (right) $\theta_0 = 60°$.

radiance to the near-solar directions, thereby slowing down the attenuation of the apparent direct solar radiation $F_{\mathrm{app}}^{\mathrm{dir}}$.

[43] Figure A2 compares, for $\theta_0 = 0°$ and $\theta_0 = 60°$, the broadband apparent direct transmission (i.e., $F_{\mathrm{app}}^{\mathrm{dir}}$ normalized by the top-of-the-atmosphere insulation) computed with the Monte Carlo model with the true direct transmission and with the estimate obtained using $k = 0.482$ in Figure A2. It is seen that although $k = 0.482$ is a slight overestimate for optically thicker clouds (Figure A1), it approximates extremely well the apparent direct transmission. In contrast, the true direct transmission is much less than the apparent transmission. Thus, if radiation scattered into near-forward directions is neglected, $F_{\mathrm{app}}^{\mathrm{dir}}$ is underestimated drastically.

[44] To compare simulated fluxes with the radiation measurements, we thus need to include near-forward scattered radiation in the "direct" flux, and remove it from the "diffuse" flux. Based on the analysis presented in Appendix A, this can be done by performing the radiative transfer calculations twice for each case: first using the actual value of τ, and second using τ multiplied by 0.48. Thus, the apparent direct and diffuse fluxes in the calculations are defined as

$$F_{app}^{\mathrm{dir}}(\tau) = F^{\mathrm{dir}}(0.48\tau) \tag{A5}$$

$$\begin{aligned} F_{\mathrm{app}}^{\mathrm{diff}}(\tau) &= F^{\mathrm{total}}(\tau) - F_{\mathrm{app}}^{\mathrm{dir}}(\tau) \\ &= \left[F^{\mathrm{dir}}(\tau) + F^{\mathrm{diff}}(\tau)\right] - F^{\mathrm{dir}}(0.48\tau) \end{aligned} \tag{A6}$$

[45] The total downward SW flux is, of course, computed using the actual value of τ. For simplicity the index "app" is omitted in the main text.

[46] **Acknowledgments.** P. Mauno, T. Nousiainen, and P. Räisänen acknowledge funding by the Academy of Finland (contracts 125180 and 127210) and M. Kahnert from the Swedish Research Council (contract 80438701). The research of G. McFarquhar was supported by the Office of Science (BER), United States Department of Energy under grants DE-FG02-02ER63337, DE-FG02-07ER64378, DE-FG02-09ER64770, and DE-SC0001279. Data were obtained from the Atmospheric Radiation Measurement program archive, sponsored by the DOE, Office of Science, Office of Biological and Environmental Research Environmental Science Division. Any opinions, findings, conclusions, or recommendations are those of the authors and do not necessarily reflect the views of the Illinois State Water Survey.

References

Anderson, G., S. Clough, F. Kneizys, J. Chetwynd, and E. Shettle (1986), AFGL atmospheric constituent profiles (0–120 km), *Tech. Rep. AFGL-TR, 86-0110*, Air Force Geophys. Lab., Hanscom Air Force Base, Bedford, Mass.

Baran, A. J., and P. N. Francis (2004), On the radiative properties of cirrus cloud at solar and thermal wavelengths: A test of model consistency using high-resolution airborne radiance, *Q. J. R. Meteorol. Soc.*, *130*, 763–778, doi:10.1256/qj.03.151.

Buschmann, N., G. M. McFarquhar, and A. J. Heymsfield (2002), Effects of observed horizontal inhomogeneities within cirrus clouds on solar radiative transfer, *J. Geophys. Res.*, *107*(D20), 4445, doi:10.1029/2001JD001273.

Dong, X., G. G. Mace, P. Minnis, W. L. Smith Jr., M. Poellot, R. T. Marchand, and A. D. Rapp (2002), Comparison of stratus cloud properties deduced from surface, GOES, and aircraft data during the March 2000 ARM Cloud IOP, *J. Atmos. Sci.*, *59*, 3265–3284, doi:10.1175/1520-0469(2002)059<3265:COSCPD>2.0.CO;2.

Ebert, E. E., and J. A. Curry (1992), A parameterization of ice cloud optical properties for climate models, *J. Geophys. Res.*, *97*(D4), 3831–3836.

Field, P. R., R. Wood, P. R. A. Brown, P. H. Kaye, E. Hirst, R. Greenaway, and J. A. Smith (2003), Ice particle interarrival times measured with a fast FSSP, *J. Atmos. Oceanic Technol.*, *20*, 249–261, doi:10.1175/1520-0426(2003)020<0249:IPITMW>2.0.CO;2.

Field, P. R., A. J. Heymsfield, and A. Bansemer (2006), Shattering and particle interarrival times measured by optical array probes in ice clouds, *J. Atmos. Oceanic Technol.*, *23*, 1357–1371, doi:10.1175/JTECH1922.1.

Fu, Q. (1996), An accurate parameterization of the solar radiative properties of cirrus clouds for climate models, *J. Clim.*, *9*, 2058–2082, doi:10.1175/1520-0442(1996)009<2058:AAPOTS>2.0.CO;2.

Fu, Q., P. Yang, and W. B. Sun (1998), An accurate parameterization of the infrared radiative properties of cirrus clouds for climate models, *J. Clim.*, *11*, 2223–2237, doi:10.1175/1520-0442(1998)011<2223:AAPOTI>2.0.CO;2.

Gardiner, B. A., and J. Hallett (1985), Degradation of in-cloud forward scattering spectrometer probe measurements in the presence of ice particles, *J. Atmos. Oceanic Technol.*, *2*, 171–180, doi:10.1175/1520-0426(1985)002<0171:DOICFS>2.0.CO;2.

Garrett, T. J., H. Gerber, D. G. Baumgardner, C. H. Twohy, and E. M. Weinstock (2003), Small, highly reflective ice crystals in low-latitude cirrus, *Geophys. Res. Lett.*, *30*(21), 2132, doi:10.1029/2003GL018153.

Gayet, J.-F., G. Febvre, and H. Larsen (1996), The reliability of the PMS FSSP in the presence of small ice crystals, *J. Atmos. Oceanic Technol.*, *13*, 1300–1310, doi:10.1175/1520-0426(1996)013<1300:TROTPF>2.0.CO;2.

Hallett, J. (2003), Measurement in the atmosphere, in *Handbook of Weather, Climate and Water: Dynamics, Climate, Physical Meteorology, Weather Systems and Measurements*, edited by T. D. Potter and B. R. Colman, pp. 711–720, John Wiley, New York.

Henyey, L. G., and J. L. Greenstein (1941), Diffuse radiation in the galaxy, *Astrophys. J.*, *93*, 70–83, doi:10.1086/144246.

Heymsfield, A. J., and L. M. Miloshevich (2003), Parameterizations for the cross-sectional area and extinction of cirrus and stratiform ice cloud particles, *J. Atmos. Sci.*, *60*, 936–956.

Heymsfield, A. J., S. Lewis, A. Bansemer, J. Iaquinta, L. M. Miloshevich, M. Kajikawa, C. Twohy, and M. R. Poellot (2002), A general approach for deriving the properties of cirrus and stratiform ice cloud particles, *J. Atmos. Sci.*, *59*, 3–29.

Hong, G., P. Yang, B. A. Baum, A. J. Heymsfield, and K.-M. Xu (2009), Parameterization of shortwave and longwave radiative properties of ice clouds for use in climate models, *J. Clim.*, *22*(23), 6287–6312, doi:10.1175/2009JCLI2844.1.

Ivanova, D., D. L. Mitchell, W. P. Arnott, and M. Poellot (2001), A GCM parameterization for bimodal size spectra and ice mass removal rates in mid-latitude cirrus clouds, *Atmos. Res.*, *59-60*, 89–113, doi:10.1016/S0169-8095(01)00111-9.

Jensen, E. P., et al. (2009), On the importance of small ice crystals in tropical anvil cirrus, *Atmos. Chem. Phys.*, *9*, 5519–5537, doi:10.5194/acp-9-5519-2009.

Kahnert, M., A. D. Sandvik, M. Biryulina, J. J. Stamnes, and K. Stamnes (2008), Impact of ice particle shape on short-wave radiative forcing: A case study for an Arctic ice cloud, *J. Quant. Spectrosc. Radiat. Transfer*, *109*, 1196–1218, doi:10.1016/j.jqrst.2007.10.016.

Kato, S., T. P. Ackerman, J. H. Mather, and E. Clothiaux (1999), The *k*-distribution method and correlated-*k* approximation for a shortwave radiative transfer model, *J. Quant. Spectrosc. Radiat. Transfer*, *62*, 109–121.

Kinne, S., T. P. Ackerman, A. J. Heymsfield, F. P. J. Valero, K. Sassen, and J. D. Spinhirne (1992), Cirrus microphysics and radiative transfer: Cloud field study on 28 October 1996, *Mon. Weather Rev.*, *120*, 661–684, doi:10.1175/1520-0493(1992)120<0661:CMARTC>2.0.CO;2.

Knollenberg, R. G., K. Kelly, and J. C. Wilson (1993), Measurements of high number densities of ice crystals in the tops of tropical cumulonimbus, *J. Geophys. Res.*, *98*(D5), 8639–8664, doi:10.1029/92JD02525.

Korolev, A. V., and G. A. Isaac (2005), Shattering during sampling by OAPs and HVPS, Part I: Snow particles, *J. Atmos. Oceanic Technol.*, *22*, 528–542, doi:10.1175/JTECH1720.1.

Korolev, A. V., E. F. Emery, J. W. Strapp, S. G. Cober, G. A. Isaac, M. Wasey, and D. Marcotte (2011), Small ice particles in tropospheric clouds: Fact or artifact? Airborne icing instrumentation evaluation experiment, *Bull. Am. Meteorol. Soc.*, *92*, 967–973, doi:10.1175/2010BAMS3141.1.

Kristjánsson, J. E., J. M. Edwards, and D. L. Mitchell (1999), A new parameterization scheme for the optical properties of ice crystals for use in general circulation models of the atmosphere, *Phys. Chem. Earth*, *24*, 231–236.

Lawson, R. P. (2011), Effects of ice particles shattering on optical cloud particle probes, *Atmos. Meas. Tech. Discuss.*, *4*, 939–968, doi:10.5194/amtd-4-939-2011.

Mace, G. G., et al. (2006), Cloud radiative forcing at the Atmospheric Radiation Measurement Program Climate Research Facility: 1. Technique,

validation, and comparison to satellite-derived diagnostic quantities, *J. Geophys. Res.*, *111*, D11S90, doi:10.1029/2005JD005921.

Macke, A., J. Mueller, and E. Raschke (1996), Single scattering properties of atmospheric ice crystals, *J. Atmos. Sci.*, *53*, 2813–2815, doi:10.1175/1520-0469(1996)053<2813:SSPOAI>2.0.CO;2.

Macke, A., P. N. Francis, G. M. McFarquhar, and S. Kinne (1998), The role of particle shapes and size distributions in the single scattering properties of cirrus clouds, *J. Atmos. Sci.*, *55*, 2874–2883.

Mayer, B., and A. Kylling (2005), Technical note: The libRadtran software package for radiative transfer calculations: Description and examples of use, *Atmos. Chem. Phys.*, *5*, 1855–1877, doi:10.5194/acp-5-1855-2005.

McFarquhar, G. M., and A. J. Heymsfield (1996), Microphysical characteristics of three anvils sampled during the Central Equatorial Pacific Experiment (CEPEX), *J. Atmos. Sci.*, *53*, 2401–2423, doi:10.1175/1520-0469(1996)053<2401:MCOTAS>2.0.CO;2.

McFarquhar, G. M., and A. J. Heymsfield (1997), Parameterization of tropical cirrus ice crystal size distributions and implications for radiative transfer: Results from CEPEX, *J. Atmos. Sci.*, *54*, 2187–2200, doi:10.1175/1520-0469(1997)054<2187:POTCIC>2.0.CO;2.

McFarquhar, G. M., A. J. Heymsfield, A. Macke, J. Iaquinta, and S. M. Aulenbach (1999), Use of observed ice crystal sizes and shapes to calculate mean-scattering properties and multispectral radiances: CEPEX April 4, 1993, case study, *J. Geophys. Res.*, *104*(D24), 31,763–31,779, doi:10.1029/1999JD900802.

McFarquhar, G. M., P. Yang, A. Macke, and A. J. Baran (2002), A new parameterization of single scattering solar radiative properties for tropical anvils using observed ice crystal size and shape distributions, *J. Atmos. Sci.*, *59*, 2458–2478, doi:10.1175/1520-0469(2002)059<2458:ANPOSS>2.0.CO;2.

McFarquhar, G. M., S. Iacobellis, and R. C. J. Somerville (2003), SCM simulations of tropical ice clouds using observationally based parameterizations of microphysics, *J. Clim.*, *16*, 1643–1664, doi:10.1175/1520-0442(2003)016<1643:SSOTIC>2.0.CO;2.

McFarquhar, G. M., M. S. Timlin, T. Nousiainen, and P. Yang (2005), A new representation of the single-scattering properties for mid-latitude clouds and its impacts, paper presented at Fifteenth Atmospheric Radiation Measurement (ARM) Science Team Meeting, Daytona Beach, Fla., 14–18 March. [Available at http://www.arm.gov/publications/proceedings/conf15/extended_abs/mcfarquhar_gm2.pdf?id=9.]

McFarquhar, G. M., J. Um, M. Freer, D. Baumgardner, G. L. Kok, and G. Mace (2007), Importance of small ice crystals to cirrus properties: Observations from the Tropical Warm Pool International Cloud Experiment (TWP-ICE), *Geophys. Res. Lett.*, *34*, L13803, doi:10.1029/2007GL029865.

McFarquhar, G. M., et al. (2011), Indirect and semi-direct aerosol campaign: The impact of Arctic aerosols on clouds, *Bull. Am. Meteorol. Soc.*, *92*, 183–201, doi:10.1175/2010BAMS2935.1.

Muinonen, K., T. Nousiainen, P. Fast, K. Lumme, and J. I. Peltoniemi (1996), Light scattering by Gaussian random particles: Ray optics approximation, *J. Quant. Spectrosc. Radiat. Transf.*, *55*, 577–601.

Nousiainen, T., and G. M. McFarquhar (2004), Light scattering by quasi-spherical ice crystals, *J. Atmos. Sci.*, *61*, 2229–2248, doi:10.1175/1520-0469(2004)061<2229:LSBQIC>2.0.CO;2.

Nousiainen, T., H. Lindqvist, G. M. McFarquhar, and J. Um (2011), Small irregular ice crystals in tropical cirrus, *J. Atmos. Sci.*, *68*, 2614–2627.

Pirazzini, R., and P. Räisänen (2008), A method to account for surface albedo heterogeneity in single column radiative transfer calculations under overcast conditions, *J. Geophys. Res.*, *113*, D20108, doi:10.1029/2008JD009815.

Ramaswamy, V., and V. Ramanathan (1989), Solar absorption by cirrus clouds and the maintenance of the tropical upper troposphere thermal structure, *J. Atmos. Sci.*, *46*, 2293–2310, doi:10.1175/1520-0469(1989)046<2293:SABCCA>2.0.CO;2.

Schlimme, I., A. Macke, and J. Reichardt (2005), The impact of ice crystal shapes, size distributions, and spatial structures of cirrus clouds on solar radiative fluxes, *J. Atmos. Sci.*, *62*, 2274–2283.

Shcherbakov, V., J.-F. Gayet, G. Febvre, A. J. Heymsfield, and G. Mioche (2010), Probabilistic model of shattering effect on in-cloud measurements, *Atmos. Chem. Phys. Discuss.*, *10*, 11,009–11,045, doi:10.5194/acpd-10-11009-2010.

Shi, Y., and C. N. Long (2002), Best estimate radiation flux value-added procedure: Algorithm operational details and explanations, *Tech. Rep. DOE/SC-ARM/TR-008*, Pac. Northwest Natl. Lab., Richland, Wash.

Shiobara, K., and S. Asano (1994), Estimation of cirrus optical thickness from Sun photometer measurements, *J. Appl. Meteorol.*, *33*, 672–681, doi:10.1175/1520-0450(1994)033<0672:EOCOTF>2.0.CO;2.

Stamnes, K., S.-C. Tsay, W. Wiscombe, and K. Jayaweera (1988), Numerically stable algorithm for discrete-ordinate-method radiative transfer in multiple scattering and emitting layered media, *Appl. Opt.*, *27*, 2502–2509, doi:10.1364/AO.27.002502.

Stephens, G. L., S.-C. Tsay, P. W. Stackhouse, and P. J. Flatau (1990), The relevance of the microphysical and radiative properties of cirrus clouds to climate and climatic feedback, *J. Atmos. Sci.*, *47*, 1742–1754, doi:10.1175/1520-0469(1990)047<1742:TROTMA>2.0.CO;2.

Stubenrauch, C. J., A. Chédin, G. Rädel, N. A. Scott, and S. Serrar (2006), Cloud properties and their seasonal and diurnal variability from TOVS path-B, *J. Clim.*, *19*, 5531–5553, doi:10.1175/JCLI3929.1.

Twohy, C. H., J. W. Strapp, and M. Wendisch (2003), Performance of a counterflow virtual impactor in the NASA Icing Research Tunnel, *J. Atmos. Oceanic Technol.*, *20*, 781–790, doi:10.1175/1520-0426(2003)020<0781:POACVI>2.0.CO;2.

Ulanowski, Z., P. Connolly, M. Flynn, M. Gallagher, A. J. M. Clarke, and E. Hesse (2004), Using ice crystal analogues to validate cloud ice parameter retrievals from the CPI ice spectrometer data, paper presented at 14th International Conference on Clouds and Precipitation, Intl. Assoc. of Meteorol. and Atmos. Sci., Bologna, Italy, 19–23 July.

Ulanowski, Z., E. Hirst, P. H. Kaye, and R. S. Greenaway (2010), Light scattering by ice particles in the Earth's atmosphere and related laboratory measurements, in *Proceedings of the 12th International Conference on Electromagnetic and Light Scattering*, pp. 294–297, Univ. of Helsinki, Helsinki, Finland.

Um, J., and G. M. McFarquhar (2009), Single-scattering properties of aggregates of plates, *Q. J. R. Meteorol. Soc.*, *135*, 291–304, doi:10.1002/qj.378.

Um, J., and G. M. McFarquhar (2011), Dependence of the single-scattering properties of small ice crystals on idealized shape models, *Atmos. Chem. Phys.*, *11*, 3159–3171.

Vidaurre, G., and J. Hallett (2009), Particle impact and breakup in aircraft measurement, *J. Atmos. Oceanic Technol.*, *26*, 972–983.

Widener, K. B, and K. Johnson (2005), Millimeter Wave Cloud Radar (MMCR) Handbook, *Tech. Rep. DOE/SC-ARM-TR-018*, U.S. Dep. of Energy, Washington, D. C.

Wylie, D. P., and W. P. Menzel (1999), Eight years of high cloud statistics using HIRS, *J. Clim.*, *12*, 170–184, doi:10.1175/1520-0442-12.1.170.

Wyser, K., and P. Yang (1998), Average ice crystal size and bulk shortwave single-scattering properties of cirrus clouds, *Atmos. Res.*, *49*, 315–335, doi:10.1016/S0169-8095(98)00083-0.

Yang, P., K. N. Liou, K. Wyser, and D. Mitchell (2000), Parametrization of the scattering and absorption properties of individual ice crystals, *J. Geophys. Res.*, *105*, 4699–4718, doi:10.1029/1999JD900755.

Yang, P., B. A. Baum, A. J. Heymsfield, Y. X. Hu, H.-L. Huang, S.-C. Tsay, and S. Ackerman (2003), Single scattering properties of droxtals, *J. Quant. Spectrosc. Radiat. Transfer*, *79-80*, 1159–1169, doi:10.1016/S0022-4073(02)00347-3.

Zhang, Y., A. Macke, and F. Albers (1999), Effect of crystal size spectrum and crystal shape on stratiform cirrus radiative forcing, *Atmos. Res.*, *52*, 59–75, doi:10.1016/S0169-8095(99)00026-5.

M. Kahnert, Swedish Meteorological and Hydrological Institute, Folkborgsvägen 1, SE-601 76 Norrköping, Sweden.

P. Mauno and T. Nousiainen, Department of Physics, University of Helsinki, PO Box 48, FI-00014 Helsinki, Finland. (paivi.mauno@helsinki.fi)

G. M. McFarquhar, Department of Atmospheric Sciences, University of Illinois at Urbana-Champaign, 105 S. Gregory St., Urbana, IL 61801-3070, USA.

P. Räisänen, Climate Change Research, Finnish Meteorological Institute, PO Box 503, FI-00101 Helsinki, Finland.

M. S. Timlin, Midwestern Regional Climate Center, CAS/ISWS/INRS, University of Illinois at Urbana-Champaign, 2204 Griffith Dr., Champaign, IL 61820, USA.